Micro-Macro Approach of Salt Viscous Fatigue under Cyclic Loading

Ahmad Pouya[1], Cheng Zhu[2], Chloé Arson[3]

[1] Lab. Navier (ENPC/IFSTTAR/CNRS), Paris-Est University, Champs sur Marne, France
[2,3] School of Civil & Environmental Engineering, Georgia Institute of Technology, Atlanta, USA

Abstract

The objective of this work is to explain the origin of fatigue observed in salt rock subject to cyclic loading. We used a self-consistent homogenization scheme to upscale the viscoplastic and damage behavior of halite polycrystals from mono-crystal viscous glide and breakage mechanisms. We modeled mono-crystals as spherical inclusions embedded in an infinite homogeneous matrix, and we assumed purely elastic inclusion/matrix interactions. We introduced a failure criterion at the mono-crystal scale in order to predict grain breakage and the subsequent damage effects on salt rock elastic moduli. We wrote an algorithm that allows computing macroscopic and microscopic stresses and strains during creep and cyclic axial loading. Although some simplifying assumptions were made in our micro- macro approach, the model provided micro-mechanical interpretations to important aspects of salt rock viscoplastic and fatigue behavior, which had not been explained so far, such as strain hardening, creep recovery, as well as damage and accelerated creep due to grain breakage. Moreover, incremental viscoplastic strains decreased over the cycles, which is in agreement with the phenomenon of "shakedown" observed in elasto-plastic media. Salt rock can be viewed as a model material. More generally, this research is expected to bring new perspectives to study the microscopic origin of fatigue in viscous polycrystalline materials.

Keywords: salt rock, visco-plasticity, fatigue, micromechanics, self-consistent method, numerical simulation

1. Introduction

The mechanical behavior of salt rock was studied extensively during the last decades for its applications to industrial problems like nuclear waste disposals [1, 2, 3, 4, 5, 6], mining [7, 8, 9], underground storage of oil and natural gas [10, 11, 12] and, more recently, Compressed Air Energy

Storage (CAES) [13]. As an aggregate of halite crystals, natural or synthetic salt has also been frequently considered as a model material to examine a variety of theoretical models of plasticity, viscoplasticity and damage in polycrystalline materials [14, 15, 16, 17, 18]. Salt cavities used for the underground storage of oil and natural gas undergo weekly to seasonal thermo-mechanical load cycles. CAES facilities are subject to shorter load cycles, of the order of a day. Experimental data shows that the resulting fatigue of salt rock (i.e., the resulting decrease of Young's modulus and strength) decreases as the load frequency increases. Fatigue is an important dimensioning factor for CAES design. However, due to the numerous variables influencing salt damage under cyclic loading (e.g., stress amplitude, loading frequency), and due to the high number of cycles necessary to assess fatigue effects in the laboratory, experimental characterization of fatigue in salt rock remains a challenge.

Mechanical properties of rocks subjected to cyclic loads differ greatly from those under static loads. Rock fatigue is largely affected by the boundary and loading conditions, such as the confining stress [19, 20], the stress/strain rate [21, 22, 23], the loading amplitude and the maximum stress [13, 24, 25, 26], as well as the type and frequency of the signal [27], and the number of cycles [28]. A review of the fatigue behavior of different types of rocks is provided in [29]. The presence of joints [30, 31], the size of grains [32], humidity conditions [22, 33] and fluid migration [34] play a critical role in the triggering and evolution of fatigue in rocks. Experimental studies of rock fatigue under cyclic loading remain scarce, and mostly focus on salt rock. Therefore, salt rock is an adequate model material to study the microscopic origin of fatigue in crystalline materials. Recently, a model of salt rock fatigue under cyclic loading was proposed in [35].

In the present paper, we analyze the origin of salt fatigue from the mechanisms of deformation of halite crystals forming the polycrystalline aggregate. Homogenization schemes were proposed to upscale microscopic gliding mechanisms in granular [36] and polycrystalline [37] media. In salt polycrystals, plastic and viscous deformation result from several fundamental mechanisms, e.g., dislocation glide, dislocation climb, polygonalization, inter-granular slip, dissolution-precipitation. Under stress and temperature typical of storage conditions, dislocation glide is the predominant mechanism that contributes to macroscopic salt rock deformation [1, 18, 38]. Dislocation glide can only occur on specific crystallographic planes, and in a limited number of directions. The non-elastic deformation of mono crystals (also called "grains" in the following) can result in geometric

incompatibilities between adjacent grains. Restricted movements within monocrystals originate internal stresses within the polycrystal. Following the micromechanical approach adopted by Pouya to study salt rock plastic behavior [39, 40], our goal is to model the viscous behavior of polycrystalline salt by upscaling viscous gliding mechanisms formulated at the crystal scale. Our study focuses on the combination of time-dependent gliding and breakage mechanisms that occur at the grain scale under cyclic loading. We presented a preliminary computational method in [41, 42]. In this paper, we propose a homogenization scheme based on Hill's incremental interaction model [43], in which we account for the heterogeneity of the elastic stiffness tensor that results from different damage mechanisms occurring at the grain scale. In order to focus on the effects of grain breakage on macroscopic viscoplastic strains, we disregard the viscous accommodation of the matrix in the inclusion-matrix interaction model. Note that in the absence of damage, this simplifying assumption yields the Kröner - Weng interaction model [44, 45]. Viscous accommodation [46, 47] falls beyond the scope of this paper. For future work, a review of incremental, secant, tangent, affine and variational formulations may be found in [48, 49, 50, 51].

In Section 2, we explain the microscopic origin of fatigue in salt rock. We present the homogenization scheme in Section 3. In Section 4, we explain a method to calculate the internal stress and damage in the polycrystal during cyclic loading. We calibrated our micro-macro model of salt viscous fatigue against creep tests reported in the literature: results are reported in Section 5. We simulated creep tests (Section 6) and cyclic loading tests (Section 7), and conducted several parametric studies in order to examine the micro-mechanical origin of fatigue.

2. Microscopic Origin of Fatigue in Salt Rock

2.1. Macroscopic Fatigue Behavior

Table A.3 in Appendix A gives an overview of the main experimental results obtained for salt rock under cyclic loading. Observations made in a variety of salt rocks are very similar. The Young's modulus and the compressive strength decrease as the number of loading cycles increase [13, 52, 53]. Fatigue initiates faster for lower loading frequency [13, 53, 54, 55]. The degradation of elastic moduli increases with the maximum stress and with the amplitude of the loading [56]. Compared to amplitude and frequency, the confining stress does not influence fatigue significantly [53]. The influence of the orientation of the bedding planes was investigated in [52]. Memory effects

in salt subject to triaxial stress states were analyzed in [57]. It has to be noted that the range of frequencies investigated in laboratory studies are significantly higher than those in actual CAES conditions. Low frequency experiments are more difficult to conduct in the laboratory, because they require more time: a sufficiently long loading period and a large number of loading cycles. Laboratory tests, performed at the macroscopic scale, were not able to reveal the microscopic origin of fatigue. The micro-macro modeling approach presented in this paper addresses this shortcoming: numerical simulations were conducted to relate the development of salt fatigue under cyclic loading to the evolution of micro-stresses in halite grains. Note that a few experimental studies relate texture development to the macroscopic strain rates of halite polycrystals subjected to creep loading [58, 59], but, to the authors' best knowledge, no such work was published on the development of textures during cyclic loading. In the absence of experimental data on the role of the lattice, we focus our micro-macro analysis of salt fatigue on visco-plastic deformation and damage that occur at the crystal scale.

2.2. Halite Crystalline Structure and Gliding Mechanisms

Halite is a Face-Centered Cubic crystal (FCC). If all constituents of the crystal were atoms, intra-granular dislocations would occur on planes separating the two densest grain fractions, i.e. on planes normal to the $< 1\,1\,1 >$ direction of the grain coordinate system. However, halite crystals comprise two FCC ionic sub-networks (sodium Na^+ and chloride Cl^-). Due to electronic interaction forces between ions, the planes along which gliding requires the minimum energy input are the $\{1\,0\,1\}$ planes (for a review of the dominant gliding mechanisms in FCC crystals, see [60, 51]). A great number of experimental studies have shown the predominance of $\{101\} < 101 >$ systems in the deformation of halite crystals (e.g., [61, 15, 62, 18, 63, 14]).

In the local coordinate system of the mono-crystal, slip systems ($\mathbf{A}^l$) are written as

$$\mathbf{A}^l = \mathbf{N}^l \otimes \mathbf{M}^l, \tag{1}$$

in which $\mathbf{N}^l$ is the vector normal to the l^{th} slip plane, $\mathbf{M}^l$ is the l^{th} unit slip vector, and $\otimes$ designates the symmetric tensor product of two vectors. The vectors normal to the preferential slip planes

are

$$\mathbf{N^1} = \frac{1}{\sqrt{2}}(0,1,1), \quad \mathbf{N^2} = \frac{1}{\sqrt{2}}(1,0,1), \quad \mathbf{N^3} = \frac{1}{\sqrt{2}}(-1,-1,0),$$
$$\mathbf{N^4} = \frac{1}{\sqrt{2}}(0,-1,1), \quad \mathbf{N^5} = \frac{1}{\sqrt{2}}(-1,0,1), \quad \mathbf{N^6} = \frac{1}{\sqrt{2}}(-1,1,0). \tag{2}$$

The slip directions are given by

$$\mathbf{M^1} = -\mathbf{N^4}, \quad \mathbf{M^2} = -\mathbf{N^5}, \quad \mathbf{M^3} = -\mathbf{N^6},$$
$$\mathbf{M^4} = -\mathbf{N^1}, \quad \mathbf{M^5} = -\mathbf{N^2}, \quad \mathbf{M^6} = -\mathbf{N^3}. \tag{3}$$

Geometrically, slip system $(\mathbf{N^4}, \mathbf{M^4})$ is orthogonal to slip system $(\mathbf{N^1}, \mathbf{M^1})$. Note that $\mathbf{A^1} = \mathbf{A^4}$, therefore both $(\mathbf{N^1}, \mathbf{M^1})$ and $(\mathbf{N^4}, \mathbf{M^4})$ yield the same strain direction. In the same way, system $(\mathbf{N^5}, \mathbf{M^5})$ (respectively $(\mathbf{N^6}, \mathbf{M^6})$) defines the same strain direction as $(\mathbf{N^2}, \mathbf{M^2})$ (respectively $(\mathbf{N^3}, \mathbf{M^3})$), because $\mathbf{A^2} = \mathbf{A^5}$ (respectively $\mathbf{A^3} = \mathbf{A^6}$). Moreover, it can be shown that:

$$\mathbf{A^1} = \mathbf{A^2} + \mathbf{A^3}. \tag{4}$$

Consequently, the 6 gliding mechanisms of the family $\{101\} < 101 >$ provide only two linearly independent slip systems for the viscous strain direction. Assuming that grain viscoplastic deformation is isochoric, the microscopic viscoplastic deformation tensor has five degrees of freedom. Since there are only two linearly independent slip systems for the family $\{101\} < 101 >$, gliding mechanisms only provide two degrees of freedom for the microscopic viscolastic tensor. This deficit in degrees of freedom results in geometric incompatibilities between adjacent grains, which originates internal stresses in the polycrystal. In fact, single NaCl crystals cannot accommodate the deformation of their neighbors by deforming viscoplastically: elastic deformation is necessary to maintain the contact with neighboring grains of different orientations. These elastic strains generate internal stresses which can in turn lead to crack propagation within the polycrystal. These internal stresses were studied by Pouya [39, 40] in elastoplasticity. In this paper, the goal is to show that the viscous behavior of salt subjected to cyclic loading can explain microscopic crack propagation, macroscopic damage and cyclic fatigue of salt rock.

In global matrix coordinates, the l^{th} slip system of the mono-crystal is noted as

$$a_{ij}^l = \frac{n_i^l m_j^l + n_j^l m_i^l}{2}, \tag{5}$$

in which $\boldsymbol{n^l}$ is the vector normal to the l^{th} slip plane, and $\boldsymbol{m^l}$ is the l^{th} unit slip vector. Moreover, the viscoplastic deformation of the grain is written as

$$\dot{\varepsilon}_{ij}^{vp} = \sum_{l=1}^{L} \dot{\gamma}^l a_{ij}^l, \tag{6}$$

in which $\dot{\gamma}^l$ is the rate of viscoplastic (shear) deformation of grains subjected to the l^{th} gliding mechanism. For halite mono-crystals, $L = 6$ (with only 2 independent gliding mechanisms). For the grain considered, $\left[\mathbf{a}^l\right]$ can be related to the l^{th} gliding mechanism expressed in the local coordinate system, $\left[\mathbf{A}^l\right]$, by means of a projection tensor $[\mathbf{P}]$ that depends on the orientation of the mono crystal:

$$\left[\mathbf{a}^l\right] = [\mathbf{P}] \left[\mathbf{A}^l\right] [\mathbf{P}]^T . \tag{7}$$

The expression of $[\mathbf{P}]$ is detailed in Appendix B. Note that contrary to previous salt plasticity models [39, 40], viscoplastic models have no threshold, therefore gliding mechanisms are all active. The local shear stress (τ^l) is related to the micro-stress ($\boldsymbol{\sigma}$) by

$$\tau^l = \boldsymbol{\sigma} : \mathbf{a}^l. \tag{8}$$

Based on the correlations established in [64, 65], we assume that the irreversible shear deformation obeys a power law as

$$\dot{\gamma}^l = \gamma_0 \, h^l \left| \frac{\tau^l}{\tau_0} \right|^n , \tag{9}$$

in which n and γ_0 are material parameters. γ_0 is a reference strain rate, and τ_0 is a reference shear stress, arbitrarily set equal to 1MPa. In the following, the model is calibrated with γ_0. h^l depends on the sign of τ^l: if τ^l is positive, $h^l = 1$; if τ^l is negative, $h^l = -1$.

3. Homogenization Scheme

3.1. Averaging Method

We consider a Representative Elementary Volume (REV) of salt rock, representing an aggregate of halite mono-crystals of different orientations. The upscaling scheme is based on averages computed in the space of crystal orientations. To determine a system of coordinates in this space, let (X, Y, Z) denote a system of crystallographic axes attached to the inclusion (Figure 1). The orientation of the Z-axis is determined by two spherical coordinates (angles Ψ and θ), defined

in the Cartesian coordinate system (x, y, z). Let (u, v, z) be the system obtained from (x, y, z) through a rotation around the z-axis by an angle Ψ. Let (U, v, Z) be the system obtained from (u, v, z) through a rotation around the v-axis by an angle θ. The system (X, Y, Z) is obtained from (U, v, Z) by an additional "spinal" rotation around the Z-axis by an angle Φ, which varies between 0 and 2π.

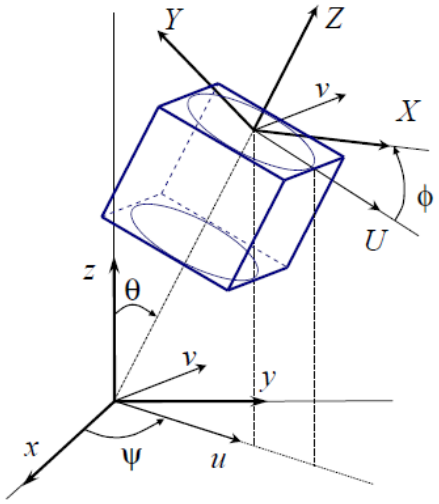

Figure 1: System of angles adopted to characterize mono crystal orientations.

The probability of having a Z-axis of orientation (Ψ, θ, Φ) is the product of the probability of occurrence of the solid angle Ω (measured by $d\Omega = sin\theta d\theta d\Psi$) by that of the spinal rotation Φ (measured by $d\Phi$). Therefore, the density of the probability of occurrence of a grain orientation ω_1 is measured by

$$dp \;=\; p(\omega_1)d\omega_1 \;=\; p(\Psi, \theta, \Phi)\, sin\theta\, d\theta d\Psi d\Phi. \tag{10}$$

Moreover, the average of a function $f(\omega_1)$ is defined as

$$\overline{f} \;=\; \frac{1}{\Omega_1}\int_{\Omega_1} f(\omega_1)d\omega_1 \;=\; \frac{1}{8\pi^2}\int_{\theta=0}^{\pi}\int_{\Psi=0}^{2\pi}\int_{\Phi=0}^{2\pi} f(\Psi, \theta, \Phi)\, sin\theta\, d\theta d\Psi d\Phi. \tag{11}$$

Salt rock is made of halite (NaCl) mono-crystals, which all have the same FCC structure. Since the inclusion (or "grain") considered represents a single crystal, crystalline symmetries allow reducing the variation of Φ to the interval $[0, \pi/2]$. Finally, changing θ to $\pi - \theta$, Ψ to $2\pi - \Psi$ and Φ to $2\pi - \Phi$ leads to the same crystallographic orientation (in which Y is changed into $-Y$). This allows reducing the domain of variation of θ to the interval $[0, \pi/2]$. Moreover, the following simulations

focus on a uniaxial macroscopic loading, in which the REV presents a symmetry about the z-axis. Therefore, Ψ can be set equal to a constant. Without reducing the generality of the model, we are considering $\Psi = 0$ in the following. As a result, in the proposed approach, the average is defined as

$$\overline{f} = \frac{2}{\pi} \int_{\theta=0}^{\pi/2} \int_{\Phi=0}^{\pi/2} f(\theta, \Phi)\, sin\theta\, d\theta d\Phi. \tag{12}$$

Using the variable change $u = cos\theta$, Equation 12 can be rewritten as

$$\overline{f} = \frac{2}{\pi} \int_{u=0}^{1} \int_{\Phi=0}^{\pi/2} f(u, \Phi)\, du d\Phi. \tag{13}$$

We assumed that all grain orientations had the same probability of occurrence, i.e. that the orientation of mono crystals followed a uniform probability density function. To obtain equipotent points in a discrete integration scheme, it is sufficient to divide the domain of variation of u ($[0, 1]$) into n_u intervals of central value u_i, and the domain of variation of Φ ($[0, \pi/2]$) into n_Φ intervals of central value Φ_j. The average is finally computed as

$$\overline{f} = \frac{1}{N} \sum_{i,j} f(\theta_i, \Phi_j), \tag{14}$$

in which $N = n_u\, n_\Phi$, and $\theta_i = Arcos(u_i)$. In the simulations presented in the following, 200 orientations were considered (i.e., $N = 200$).

3.2. Inclusion-Matrix Interaction Model

The stresses and strains in mono-crystals depend on the macroscopic load imposed to the aggregate REV, and on the interactions between these mono-crystals. We used a simplified "inclusion-matrix model" to account for the interaction between grains. Following a self-consistent upscaling scheme, each mono-crystal is viewed as an inclusion embedded in an infinite homogeneous matrix, which represents the polycrystalline aggregate. The behavior of the matrix is *a priori* unknown. Therefore, the upscaling method is based on an implicit system of equations: the unknown matrix model has to be determined iteratively. Macroscopic properties such as the effective elastic tensor are deduced from the knowledge of stress or strain concentration tensors, which depend on the geometry of the heterogeneity present in the aggregate [66, 67]. We modeled mono-crystals as spherical inclusions (Figure 2). A more sophisticated inclusion shape (e.g., ellipsoidal, needle-shaped, and disk-shaped) could have been accounted for in the homogenization scheme [68, 69]. However, no significant grain anisotropy has ever been evidenced by experimental microstructure

observations or mechanical tests with contrast, for instance, to laminated metals, which are known to exhibit highly anisotropic texture (i.e., elongated grain shapes). This difference may be due to the genesis mechanism of the crystals involved in salt microstructure. These crystals grow in supersaturated brine, as water evaporates. This process does not result in preferential growth direction. Therefore, we used a spherical inclusion shape and we used Hill's incremental inclusion-matrix model [43] to build up our homogenization method. In Hill's model, small variations of the local stress in the inclusions ($\boldsymbol{\sigma}$) and small variations of the far-field stress in the matrix ($\overline{\boldsymbol{\sigma}}$) are coupled to those of the microscopic strain ($\boldsymbol{\varepsilon}$) and those of the macroscopic strain ($\overline{\boldsymbol{\varepsilon}}$) by the following relationship:

$$\delta\boldsymbol{\sigma} - \delta\overline{\boldsymbol{\sigma}} = -\boldsymbol{L}^{*} : (\delta\boldsymbol{\varepsilon} - \delta\overline{\boldsymbol{\varepsilon}}), \tag{15}$$

in which $\boldsymbol{L}^{*}$ is Hill's tensor. For a spherical inclusion in an isotropic elastic matrix [43], $\boldsymbol{L}^{*}$ is given by

$$L^{*}_{ijkl} = \frac{\mu}{4-5\nu}\left[(3-5\nu)\delta_{ij}\delta_{kl} + \frac{7-5\nu}{2}(\delta_{ik}\delta_{jl} + \delta_{il}\delta_{jk})\right], \tag{16}$$

in which μ and ν are respectively the shear modulus and Poisson's ratio of the matrix. If the elastic properties of the aggregate are uniform (same elastic properties for all the grains) and if damage is not considered, then this model yields the so called Kröner-Weng model, proposed initially by Kröner [44] for elastic-plastic materials and extended by Weng for viscoplastic materials [45] (Appendix C). In Kröner-Weng's model, the matrix-inclusion interaction is assumed to be purely elastic, which implies that macroscopic viscoplasticity only stems from grain-scale viscoplastic deformation, and not from grain/matrix incompatibilities that originate a viscous "accommodation" of the matrix around the inclusion. It is well known that this simplifying assumption leads to a too stiff matrix. More sophisticated models were proposed to take the viscous deformation of the matrix into account in the inclusion-matrix model [46, 47, 48, 49]. In this paper, we focus on the damage effects coupled with viscous deformation of the aggregate. We neglect viscous accommodation in order to better understand the effects of damage in the inclusion-matrix interaction model. Damage is assumed to be the result of grain breakage, which implies that broken grains are replaced by inclusions with no stiffness whereas non-broken grains keep the same elastic stiffness. Note that Kröner-Weng model was obtained by assuming that the same elastic tensor could be used for all the inclusions, as well as for the matrix. In the following section we explain how brittle damage at the grain scale is taken into account in the homogenization method.

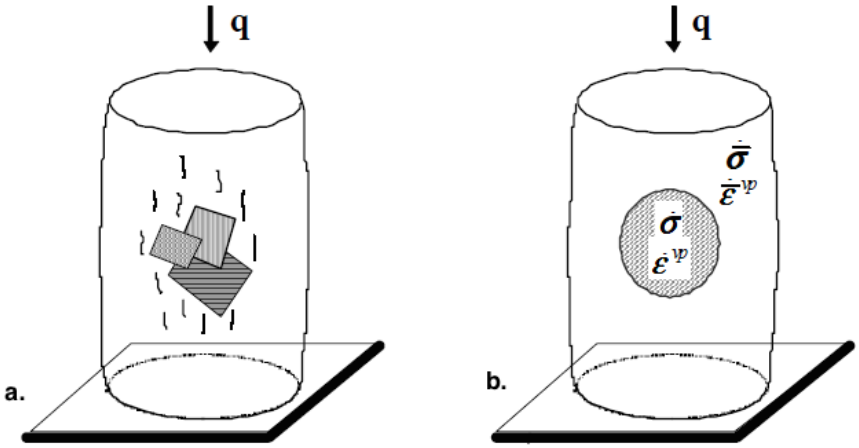

Figure 2: Salt rock Representative Elementary Volume (REV). a. Monocrystal inclusions in the homogeneous matrix. b. Schematic representation of salt mono-crystals in the inclusion-matrix model.

3.3. Micro-macro Deformation and Damage Modeling

At the REV scale, damage is defined as the reduction of elastic moduli and rock strength. Macroscopically, crack propagation in a rock REV can be driven by tension, compression or shear [70, 71]. In our model, we replace the initiation of a crack at the grain-matrix interface or inside the grain by the breakage of the whole grain. Therefore, at the grain scale, damage triggers when one mono-crystal fails. Microscopically, we restrict the initiation of damage at the grain scale to mode I failure, which occurs when the microscopic stress exceeds the tensile strength of salt mono-crystals (equal to 2MPa, see [40]). In our model, if the major principal local stress of a grain exceeds 2 MPa, the grain is breaking. More sophisticated models of progressive grain damage would be more appropriate to account for the anisotropy induced by diffuse crack propagation in the polycrystal. Anisotropy induced by the propagation of parallel micro-cracks was modeled in a homogenization scheme proposed in [72]: strain-softening in tension is accounted for thanks to a linear-fracture-mechanics-based single-crack propagation criterion, which is coupled with a Mori-Tanaka inclusion-matrix model. Stiffness reduction is captured for small values of damage. In the self-consistent method adopted in this paper, representing cracks explicitly would require modeling crack propagation within spherical grain inclusions embedded in an infinite matrix. Because loading is anisotropic, anisotropic damage at the grain scale (e.g., single crack propagation in a grain) would result in an anisotropic matrix behavior, which, for consistency, should be translated into a

specific Hill's tensor expressed for an anisotropic matrix. To our best knowledge, homogenization schemes proposed so far (including that proposed in [72]) resort to the expression of Hill's tensor for an isotropic matrix. This paper focuses on the coupling between damage and viscous behavior, therefore the model was formulated with grains considered as perfectly brittle spherical inclusions: we model a grain "breakage" mechanism, as opposed to a (microscopic) grain "damage" mechanism. Macroscopic damage propagates when subsequent stress redistribution and further loading bring micro-stress in other grains to the tensile limit. The number of unbroken grains is noted N_g, the number of broken grains is noted N_b, and the total number of grains in the REV is noted N (with $N = n_u\, n_\Phi$, the number of mono-crystal orientations considered in the REV). The Voigt estimate for the elastic matrix yields the following effective bulk modulus ($\widetilde{\kappa}$) and shear modulus ($\widetilde{\mu}$) as

$$\widetilde{\kappa} = \frac{N_g}{N}\kappa = \frac{N - N_b}{N}\kappa = (1 - D)\kappa, \qquad \widetilde{\mu} = \frac{N_g}{N}\mu = \frac{N - N_b}{N}\mu = (1 - D)\mu, \tag{17}$$

in which the damage variable is defined as $D = N_b/N = 1 - N_g/N$. From the expressions of the damaged bulk and shear moduli in Equation 17, it can be shown that Poisson's ratio does not change upon grain breakage: $\widetilde{\nu} = \nu$. The micro-macro modeling approach proposed here combines Hill's scheme [43] for the rate-independent non linear elastic matrix behavior (to represent the inclusion-matrix interaction), and a brittle constitutive law for the grains subject to breakage (to represent damage). Hill's constraint tensor is calculated for the damaged matrix. So, in the present work, the inclusion-matrix interaction model accounts for brittle grain breakage, but does not capture the "viscous accommodation" due to the viscous deformation of the matrix. This simplification is considered acceptable for the sake of this study, which focuses on macroscopic fatigue behavior induced by cyclic loading.

For each macroscopic stress loading increment $\delta q(t)$ applied between times t_n and t_{n+1}, the macroscopic and microscopic variables are updated in two steps, as illustrated in Figure 3:

1. The "damage phase" ($t_n \sim t_n^+$) accounts for instantaneous variations due to grain breakage at time t_n: these variations are noted $\delta\boldsymbol{\sigma}$, $\delta\boldsymbol{\varepsilon}$, $\delta\overline{\boldsymbol{\sigma}}$, $\delta\overline{\boldsymbol{\varepsilon}}$.
2. The "viscous phase" ($t_n^+ \sim t_{n+1}$): accounts for time-dependent variations due to viscous deformation on the time interval $\Delta_n t = t_{n+1} - t_n$: these variations are noted $\dot{\sigma}\Delta_n t$, $\dot{\varepsilon}\Delta_n t$, $\dot{\overline{\boldsymbol{\sigma}}}\Delta_n t$, $\dot{\overline{\boldsymbol{\varepsilon}}}\Delta_n t$, in which: $\dot{\boldsymbol{\sigma}}$ is the rate of microscopic stress, $\dot{\overline{\boldsymbol{\sigma}}}$ is the rate of macroscopic stress, $\dot{\overline{\boldsymbol{\varepsilon}}}$ is the macroscopic strain rate, and $\dot{\boldsymbol{\varepsilon}}$ is the microscopic strain rate.

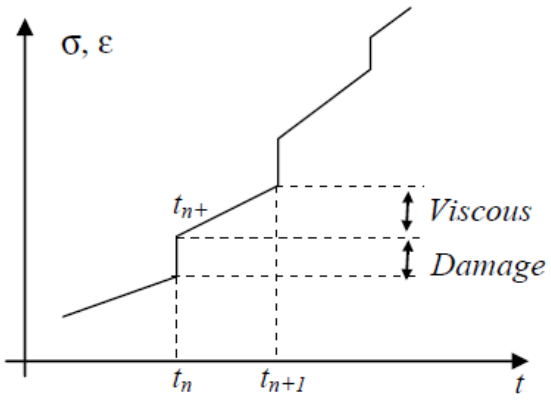

Figure 3: Stress computational method: decomposition of the time step into damage and viscous phases, for stress- or strain- controlled tests.

At each stress increment (i.e., time step), the grain breakage criterion is checked at the beginning of the damage phase ($t = t_n$). Grains are sorted into three categories, depending on the stress state of the mono-crystal considered:

- The grain is non-broken if the maximum principal microscopic stress is less than the mono-crystal tensile strength of 2 MPa;
- The grain is breaking if the maximum principal microscopic stress exceeds the mono-crystal tensile strength of 2 MPa during the current loading increment;
- The grain is broken if the mono-crystal had already broken in a previous loading increment.

Initially at $t = t_n$, the damaged elastic moduli are calculated from Equation 17, in which N_b accounts for both breaking and broken grains. For all types of grains, the inclusion-matrix interaction is governed by Hill's formulae (Equation 15). Grain breakage results in a redistribution of micro-stresses: when breaking grains actually fail, non-broken grains become subjected to microscopic stresses of higher magnitude (details are provided in Section 4.1). At the beginning of the viscous phase (at $t = t_n^+$), resulting micro-stresses are updated by using the equations governing the gliding mechanisms. Note that the redistribution of micro-stresses due to grain breakage (at $t = t_n^+$) can result in tensile stresses that exceed the tensile strength in some of the non-broken grains. Grains that are subjected to higher stresses than the tensile strength are considered as non-broken during the viscous phase of the loading (between $t = t_n^+$ and $t = t_{n+1}$), and the status of the grains is

checked and updated at the beginning of the damage phase of the following loading increment (at $t = t_{n+1}$).

4. Micro-Macro Stress Computational Method

4.1. Stress Redistribution due to Damage

By definition, the macroscopic stress (respectively strain) is the average of microscopic stresses (respectively strains). Other averaged local quantities are not necessarily equal to the corresponding macroscopic quantities. For instance, the macroscopic viscoplastic strain is the average of the microscopic viscoplastic strains, only if the elastic tensor is uniform or homogeneous. In the present modeling approach, macroscopic damage is caused by the breakage of the grains where microscopic tensile stress is the highest. In general, the spatial distribution of broken grains is not uniform. Therefore the macroscopic viscous strain is not the average of the local viscous strain: $< \boldsymbol{\varepsilon}^{vp} > \neq \overline{\boldsymbol{\varepsilon}}^{vp}$. This difference can be shown by using different stiffness tensors for different grains in Equation 15.

We assumed that the microscopic stress in a broken grain vanishes, which corresponds to a perfectly brittle failure. The elastic moduli of broken grains are assigned a zero value, and broken grains are modeled as void inclusions in the matrix. When the REV is subjected to a macroscopic stress at its boundary, the whole matrix deforms, and these void inclusions deform as well. By definition, $\delta\overline{\boldsymbol{\sigma}} = \boldsymbol{C} : \delta\overline{\boldsymbol{\varepsilon}}$, where the damaged elasticity tensor of the matrix ($\boldsymbol{C}$) is related to the elasticity tensor of non-broken grains ($\boldsymbol{C_0}$) as

$$\boldsymbol{C} = (1 - D)\boldsymbol{C_0}. \tag{18}$$

The breaking and broken grains have no stiffness, and are both subjected to zero microstress, therefore $D(t_n) = N_b(t_n)/N$ in which $N_b(t_n) = N - N_g(t_n)$. The damaged elastic properties are updated as

$$\mu(t_n) = (1-D(t_n))\,\mu(t_0) = \frac{N_g(t_n)}{N}\mu(t_0), \quad \kappa(t_n) = (1-D(t_n))\,\kappa(t_0) = \frac{N_g(t_n)}{N_T}\kappa(t_0), \quad \nu(t_n) = \nu(t_0), \tag{19}$$

in which $\mu(t_0)$, $\kappa(t_0)$, $\nu(t_0)$ are the elastic properties of the undamaged matrix. The change of microscopic deformation ($\delta\boldsymbol{\varepsilon}$) is obtained by combining Equation 15 with the expression of the change of microscopic stress ($\delta\boldsymbol{\sigma}$). Each type of grain undergoes a different change of microscopic

stress during the damage phase of the loading increment: $\delta\boldsymbol{\sigma} = \boldsymbol{C_0} : \delta\boldsymbol{\varepsilon}$ for non-broken grains, $\delta\boldsymbol{\sigma} = -\boldsymbol{\sigma}$ for breaking grains and $\delta\boldsymbol{\sigma} = 0$ for broken grains. The resulting expressions of the change of microstress is given in Table 1 for each type of grain.

Table 1: Microscopic stress change due to grain breakage.

	Microscopic stress	Microscopic deformation
Non-broken grains	$\delta\boldsymbol{\sigma} = \boldsymbol{C_0} : \delta\boldsymbol{\varepsilon}$	$\delta\boldsymbol{\varepsilon} = [\boldsymbol{I} + \boldsymbol{M^*} : \boldsymbol{C_0}]^{-1} : (\delta\overline{\boldsymbol{\varepsilon}} + \boldsymbol{M^*} : \delta\overline{\boldsymbol{\sigma}})$
Breaking grains	$\delta\boldsymbol{\sigma} = -\boldsymbol{\sigma}$	$\delta\boldsymbol{\varepsilon} = \boldsymbol{M^*} : \boldsymbol{\sigma} + \delta\overline{\boldsymbol{\varepsilon}} + \boldsymbol{M^*} : \delta\overline{\boldsymbol{\sigma}}$
Broken grains	$\delta\boldsymbol{\sigma} = 0$	$\delta\boldsymbol{\varepsilon} = \delta\overline{\boldsymbol{\varepsilon}} + \boldsymbol{M^*} : \delta\overline{\boldsymbol{\sigma}}$
Notation:	$\boldsymbol{M^*} = \boldsymbol{L^{*-1}}$	$I_{ijkl} = \frac{1}{2}(\delta_{ik}\delta_{jl} + \delta_{il}\delta_{jk})$

For the special case of stress-controlled loading paths studied here, the variation of macroscopic stress is applied during the viscous phase of the loading ($t_n^+ \sim t_{n+1}$). Therefore, during the damage phase: $\delta\overline{\boldsymbol{\sigma}} = 0$. Therefore, the variations of microscopic deformation during the damage phase of the time step are given by

$$\begin{aligned} \text{Non-broken grain:} \quad & \delta\boldsymbol{\varepsilon} = [\boldsymbol{I} + \boldsymbol{M^*} : \boldsymbol{C_0}]^{-1} : \delta\overline{\boldsymbol{\varepsilon}}, \\ \text{Breaking grain:} \quad & \delta\boldsymbol{\varepsilon} = \boldsymbol{M^*} : \boldsymbol{\sigma} + \delta\overline{\boldsymbol{\varepsilon}}, \\ \text{Broken grain:} \quad & \delta\boldsymbol{\varepsilon} = \delta\overline{\boldsymbol{\varepsilon}}. \end{aligned} \tag{20}$$

Recalling that $\delta\overline{\boldsymbol{\varepsilon}} =< \delta\boldsymbol{\varepsilon} >$, at time t_n^+, Equations 20 can be rewritten as

$$\begin{aligned} N\delta\overline{\boldsymbol{\varepsilon}} \;=\; & \sum_{\text{non-broken}} [\boldsymbol{I} + \boldsymbol{M^*} : \boldsymbol{C}_0]^{-1} : \delta\overline{\boldsymbol{\varepsilon}} \\ + \; & \sum_{\text{breaking}} \boldsymbol{M^*} : \boldsymbol{\sigma} + \sum_{\text{breaking}} \boldsymbol{I} : \delta\overline{\boldsymbol{\varepsilon}} \\ + \; & \sum_{\text{broken}} \boldsymbol{I} : \delta\overline{\boldsymbol{\varepsilon}}. \end{aligned} \tag{21}$$

The variation of macroscopic strain $\delta\overline{\boldsymbol{\varepsilon}}$ is obtained from Equation 21 as

$$\delta\overline{\boldsymbol{\varepsilon}} = \frac{1}{N_g(t_n)}[\boldsymbol{I} - (\boldsymbol{I} + \boldsymbol{M^*} : \boldsymbol{C_0})^{-1}]^{-1} : [\boldsymbol{M^*} : (\sum_{\text{breaking}} \boldsymbol{\sigma})]. \tag{22}$$

Then $\delta\boldsymbol{\varepsilon}$ and $\delta\boldsymbol{\sigma}$ can be updated for each type of grain (according to the equations listed in Table 1). It should be noted that at the end of the damage phase (at $t = t_n^+$), there are only two types of grains: non-broken and broken (the breaking grains become counted as part of the broken grains). Broken grains are considered as voids, with: $\boldsymbol{\sigma}(t_n^+) = 0$, $\dot{\boldsymbol{\sigma}}(t_n^+) = 0$, $\dot{\boldsymbol{\varepsilon}}^{vp}(t_n^+) = 0$.

In summary, in the damage phase of each loading increment, calculations are performed in the following order:

$$\boldsymbol{\sigma}(t_n) \rightarrow \left\{ \begin{array}{r} < 2 \text{ MPa : grain is non-broken} \\ \geq 2 \text{ MPa : grain is breaking} \\ \text{broken grains remain broken} \end{array} \right\} \rightarrow \begin{array}{l} N_g(t_n) \\ N_b(t_n) \end{array} \rightarrow \widetilde{\mu}(t_n) \xrightarrow{\boldsymbol{\sigma}(t_n)} \delta\overline{\boldsymbol{\varepsilon}}(t_n) \rightarrow \delta\boldsymbol{\varepsilon}(t_n) \rightarrow \delta\boldsymbol{\sigma}(t_n) \rightarrow \boldsymbol{\sigma}(t_n^+)$$

4.2. Stress Redistribution due to Viscoplasticity

At the beginning of the viscous phase (at $t = t_n^+$ in Figure 3), the following variables are known:

- At the macroscopic scale: $p(t_n^+)$, $q(t_n^+)$, $\overline{\boldsymbol{\sigma}}(t_n^+)$, $\overline{\boldsymbol{\varepsilon}}^{vp}(t_n^+)$, $\overline{\boldsymbol{\varepsilon}}(t_n^+)$, $\mu(t_n^+)$, $\nu(t_n^+) = \nu(t_0)$, $\boldsymbol{C}(t_n^+)$, $\boldsymbol{L}^*(t_n^+)$, $N_g(t_n^+) = N_g(t_n)$, $N_b(t_n^+) = N_b(t_n)$
- At the microscopic scale: $\boldsymbol{\sigma}(t_n^+)$, $\boldsymbol{\varepsilon}^{vp}(t_n^+)$, $\boldsymbol{\varepsilon}(t_n^+)$

Viscous loading phase for the grains that are non-broken at time $t = t_n^+$.

The microscopic stress $\boldsymbol{\sigma}(t_n^+)$ is used to calculate the viscoplastic strain rate at the grain scale:

$$\dot{\gamma}^l(t_n^+) \;=\; \gamma_0\, h^l \left| \frac{\tau^l(t_n^+)}{\tau_0} \right|^n \;=\; \gamma_0\, h^l \left| \frac{\boldsymbol{\sigma}(t_n^+) : \boldsymbol{a^l}}{\tau_0} \right|^n \quad \Rightarrow \quad \dot{\boldsymbol{\varepsilon}}^{vp}(t_n^+) \;=\; \sum_{l=1}^{6} \dot{\gamma}^l(t_n^+) \boldsymbol{a}^l. \tag{23}$$

The macroscopic loading rate $\dot{\overline{\boldsymbol{\sigma}}}(t_n^+)$ is assumed to be given; it depends on the type of loading considered, creep or sinusoidal cyclic loading. After replacing small variations by rates in Equation 15, and after some computations, the microscopic stress rate $\dot{\boldsymbol{\sigma}}(t_n^+)$ can be expressed as

$$\begin{aligned} (\boldsymbol{I} + \boldsymbol{L^*}(t_n^+) : \boldsymbol{C_0^{-1}}) : \dot{\boldsymbol{\sigma}}(t_n^+) \;=\; & (\boldsymbol{I} + \boldsymbol{L^*}(t_n^+) : \boldsymbol{C^{-1}}(t_n^+)) : \dot{\overline{\boldsymbol{\sigma}}}(t_n^+) \\ & + \boldsymbol{L^*}(t_n^+) : (\dot{\overline{\boldsymbol{\varepsilon}}}^{vp}(t_n^+) - \dot{\boldsymbol{\varepsilon}}^{vp}(t_n^+)). \end{aligned} \tag{24}$$

The cumulated macroscopic stress at $t = t_{n+1}$ is calculated as

$$\boldsymbol{\sigma}(t_{n+1}) = \boldsymbol{\sigma}(t_n^+) + \dot{\boldsymbol{\sigma}}(t_n^+) \times \Delta_n t. \tag{25}$$

For non-broken grains, variables $\overline{\boldsymbol{\sigma}}(t_{n+1})$, $\overline{\boldsymbol{\varepsilon}}^{vp}(t_{n+1})$, $\overline{\boldsymbol{\varepsilon}}(t_{n+1})$, $\boldsymbol{\varepsilon}^{vp}(t_{n+1})$ are obtained by time integration (similar to Equation 25). The microstress in non-broken grains is compared to the tensile strength of the mono-crystal at the following loading increment.

Viscous loading phase for the grains that are broken at time $t = t_n^+$.

Grains that are already broken at time $t = t_n^+$ are replaced by voids, i.e. by stress-free cavities with zero stiffness. Gliding mechanisms are no longer active in broken grains, so that: $\boldsymbol{\sigma}(t_{n+1}) = \boldsymbol{\sigma}(t_n^+) = 0$, $\dot{\boldsymbol{\sigma}}(t_{n+1}) = \dot{\boldsymbol{\sigma}}(t_n^+) = 0$, $\dot{\boldsymbol{\varepsilon}}^{vp}(t_{n+1}) = \dot{\boldsymbol{\varepsilon}}^{vp}(t_n^+) = 0$. Then the total strain rate of the broken grain (i.e. the deformation rate of the hole) is computed as

$$\dot{\boldsymbol{\varepsilon}}(t_n^+) = \boldsymbol{S}_D(t_n^+) : \dot{\overline{\boldsymbol{\sigma}}}(t_n^+), \tag{26}$$

in which $\dot{\overline{\boldsymbol{\sigma}}}(t_n^+)$ is given by the type of macroscopic loading considered. Moreover, $\boldsymbol{S}_D(t_n^+) = \boldsymbol{L^*}^{-1}(t_n^+) + \boldsymbol{C}^{-1}(t_n^+)$.

In summary, in the viscous phase of each loading increment, calculations are performed in the following order:

$$\begin{matrix} \dot{\overline{\boldsymbol{\sigma}}}(t_n^+) \\ \widetilde{\mu}(t_n^+) = \widetilde{\mu}(t_n) \end{matrix} \rightarrow \left\{ \begin{matrix} \dot{\overline{\boldsymbol{\varepsilon}}}^{\boldsymbol{vp}}(t_n^+) \\ \dot{\gamma}^l(t_n^+) \rightarrow \dot{\boldsymbol{\varepsilon}}^{\boldsymbol{vp}}(t_n^+) \end{matrix} \right\} \rightarrow \dot{\boldsymbol{\sigma}}(t_n^+) \xrightarrow{\boldsymbol{\sigma}(t_n^+)} \boldsymbol{\sigma}(t_{n+1})$$

4.3. Computational method for axial loading

The computational method can be used to determine micro-stresses in an aggregate subjected to axial macroscopic loading. We note, for a macroscopic axial loading along the $\mathbf{e_3}$ axis:

$$\overline{\boldsymbol{\sigma}} = q(t)\mathbf{r}, \quad \overline{\mathbf{s}} = \overline{\boldsymbol{\sigma}} - \frac{Tr(\overline{\boldsymbol{\sigma}})}{3}\boldsymbol{\delta} = q(t)\boldsymbol{\Psi}, \quad \dot{\overline{\boldsymbol{\varepsilon}}}^{vp} = \frac{3}{2}\dot{p}(t)\boldsymbol{\Psi}, \tag{27}$$

in which:

$$\mathbf{r} = -\mathbf{e_3} \otimes \mathbf{e_3}, \qquad \boldsymbol{\Psi} = \mathbf{r} - \frac{1}{3}Tr(\mathbf{r})\boldsymbol{\delta}. \tag{28}$$

The loading rate $\dot{q}$ at time t_n^+ is calculated according to the type of loading considered:

- For a creep loading test:

$$\dot{q}(t_0) = \infty, \quad \dot{q}(t_n^+, t_n \neq t_0) = 0 \tag{29}$$

- For a sinusoidal cyclic loading test:

$$\dot{q}(t_n^+) = q_0\omega cos(\omega t_n) \tag{30}$$

We introduce the following notation:

$$\dot{\rho}(t) = \dot{q}(t) + 3\mu(1-\beta)\dot{p}(t), \tag{31}$$

in which β is given by:

$$\beta \;=\; \frac{2(4-5\nu)}{15(1-\nu)} \tag{32}$$

The value of $\dot{\rho}$ is obtained from $N_g(t_n^+)$ (calculated during the damage phase), and from Equations 29-30:

$$\dot{\rho}(t_n^+) = \dot{q}(t_n^+) + 3\mu(t_n^+)(1-\beta(t_n^+)) < \dot{\boldsymbol{\varepsilon}}^{vp}(t_n^+) >: \boldsymbol{\Psi}, \tag{33}$$

from which, the rate of macroscopic viscoplastic strain can be obtained as

$$\dot{p}(t_n^+) = \frac{\dot{\rho}(t_n^+) - \dot{q}(t_n^+)}{3\mu(t_n^+)[1-\beta(t_n^+)]} =< \dot{\boldsymbol{\varepsilon}}^{vp}(t_n^+) >: \boldsymbol{\Psi} \quad \Rightarrow \quad \dot{\bar{\boldsymbol{\varepsilon}}}^{vp}(t_n^+) = \frac{3}{2}\dot{p}(t_n^+)\boldsymbol{\Psi}. \tag{34}$$

The simulations presented in the following are based on Equations 27-34 for an axial loading.

5. Model Calibration against Creep Tests

We determined the model parameters by calibrating the following relationship, which we derived from the equations of the micro-macro approach presented above:

$$\dot{p}(t) \;=\; \frac{M}{3\mu(1-\beta)}\,\frac{q^n(t)}{(\tau_0)^n}, \tag{35}$$

in which:

$$M \;=\; 3\mu(1-\beta)\langle \sum_{l=1}^{L} \gamma_0 \left| \mathbf{r} : \mathbf{a}^l \right|^{n+1} \rangle. \tag{36}$$

The details of the derivations are provided in Appendix D. Note that an approximation was made: in Equations 6 and 9, the microscopic stress $\boldsymbol{\sigma}$ was replaced by the macroscopic stress $\overline{\boldsymbol{\sigma}} = q(t)\mathbf{r}$. The advantage of the form of relationship given by Equation 35 is that it directly relates the macroscopic viscoplastic strain rate to the macroscopic stress imposed in the simulations. Therefore, it is convenient to use it for calibration purposes. After calibration, it was verified that the variations of the macroscopic viscoplastic strains predicted by the approximate law in Equation 35 followed those predicted by the non-approximated micro-macro model with less than 5% error (the verifications are not presented here, for the sake of brevity).

The microscopic constitutive law in Equation 9 depends on two parameters: γ_0 and n. In addition, parameters μ and β depend on the macroscopic elastic properties of the polycrystal in the reference state. The Poisson's ratio is not affected by damage in the proposed model. That is why it was not calibrated: a standard value of $\nu_0 = 0.3$ was adopted. The polycrystal Young's

modulus was also given a value typical of rock salt [13]: E_0=23 GPa. The calibration procedure was based on a genetic algorithm that selects the set of parameters that minimizes the difference between points of experimental and numerical creep curves. The asymptotic strain rates at the end of the 7-hour and 30-day creep tests reported in [13] were computed for each loading condition considered, and were used as reference data. The distance between the reference and simulated curves was computed with a Least Square Method. The best fit for the short- and long-term creep tests provided the optimal values of γ_0 and n, reported in Table 2.

Table 2: Model parameters calibrated against creep tests reported in [13].

Creep Test	γ_0 (day^{-1})	n (-)
Short Term (7 hours)	5.17×10^{-4}	3.58
Long Term (30 days)	2.93×10^{-5}	4.04

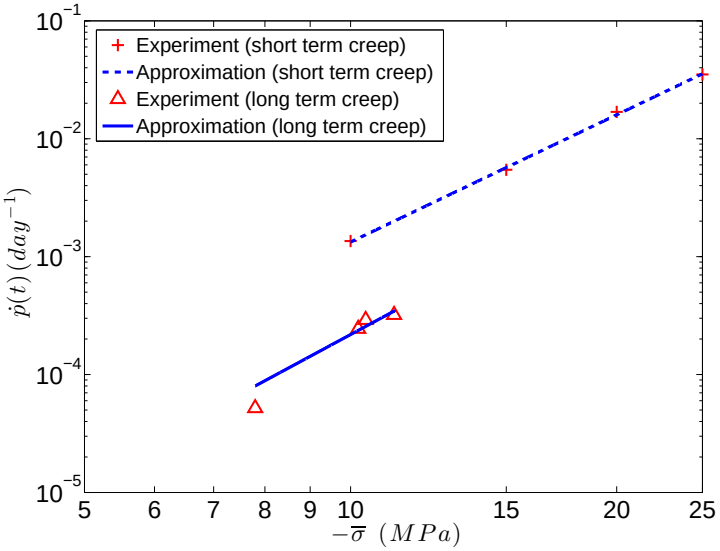

Figure 4: Calibration of the approximated macroscopic creep law against creep tests reported in [13]. Constant loading stress for short-term creep: 10, 15, 20, 25 MPa. Constant loading stress for long-term creep: 7.8, 10.2, 10.4, 11.2 MPa.

6. Influence of Microscopic Creep and Grain Breakage on Macroscopic Creep Regimes

6.1. Microscopic Origin of Creep Recovery

Two long-term creep tests were simulated with the following parameters: $\gamma_0 = 2.93\times10^{-5}\,\text{day}^{-1}$, $n = 4.04$. First, grain breakage was not accounted for, which implies that macroscopic viscoplastic deformation was solely due to microscopic viscoplastic strains. The stress paths for both tests are illustrated in Figure 5.a. In the first test, a constant macroscopic stress of 7 MPa was maintained for three days. The second test included the four following phases: (1) an instantaneous axial stress loading from 0 MPa to 7 MPa, (2) a creep phase under a constant stress of 7MPa, maintained for about half a day, (3) an instantaneous stress unloading, from 7 MPa to 1 MPa, and (4) a creep phase under a constant stress of 1 MPa, maintained for about two and half days. The evolution of total macroscopic strains is shown in Figure 5.b.

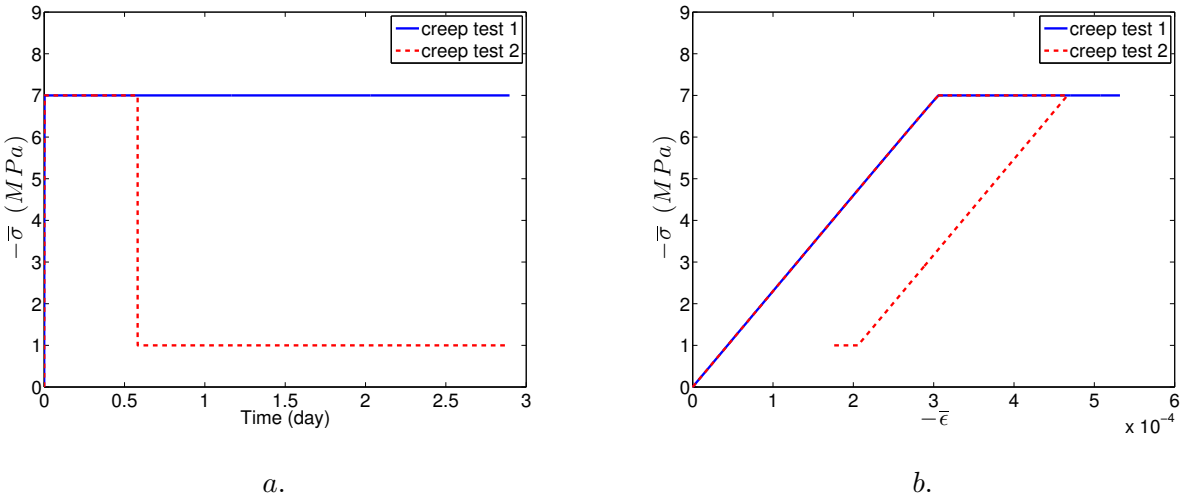

a. *b.*

Figure 5: Simulation of two long-term creep tests. In the first test, a macroscopic stress of 7 MPa is maintained for three days. In the second test, the stress path is the following: (a) Instantaneous loading from 0 MPa to 7 MPa, stress plateau of 7 MPa maintained half a day, unloading from 7 MPa to 1 MPa, stress plateau of 1 MPa maintained two and half days. (b) Corresponding evolution of total macroscopic strains.

As expected, macroscopic viscoplastic strains do not vary during the instantaneous loading and unloading phases (Figure 6.a). In the first creep test, the macroscopic strain rate decreases (from B to C, and from C to E), which illustrates the macroscopic strain hardening noted in most experiments. Note that there is no hardening in the creep model adopted at the grain scale;

therefore, the hardening at the macro level is due to the interaction between the grains and the polycrystal. For extended periods of time, the strain rate tends asymptotically to zero: Figure 7, from E to F, illustrates the asymptotic creep behavior over 180 days. After the unloading phase simulated in the second creep test (i.e., after point D in Figure 6.b), the macroscopic strain rate is positive, which indicates that the specimen is in extension, although the macroscopic load imposed during phase 4 of test 2 is a compression. This phenomenon, named "creep recovery", is a kind of memory effect [57], which was observed experimentally [73, 74], and modeled phenomenologically. For instance, Munson and Dawson [2] introduced *ad hoc* parameters explicitly in their formulation to match model predictions with experimental data. Qualitative explanations based on internal stresses were sometimes invoked by researchers, but the cause of creep recovery was not well explained. In our micro-macro approach, creep recovery is automatically captured, as a model output. The method is powerful, because results confirm that the origin of recovery actually stems from grain viscoplastic deformation and grain interactions within the polycrystal.

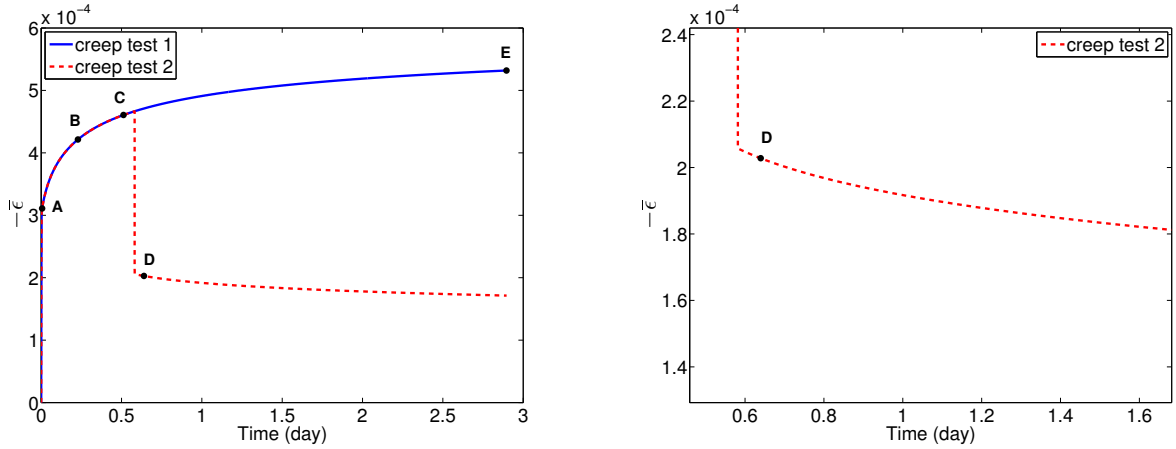

a. *b.*

Figure 6: Evolution of macroscopic strains during the two long-term creep tests (grain breakage was not accounted for). (a) Evolution of total strains with time. (b) Zoom of the time evolution of macroscopic strains in the second creep test.

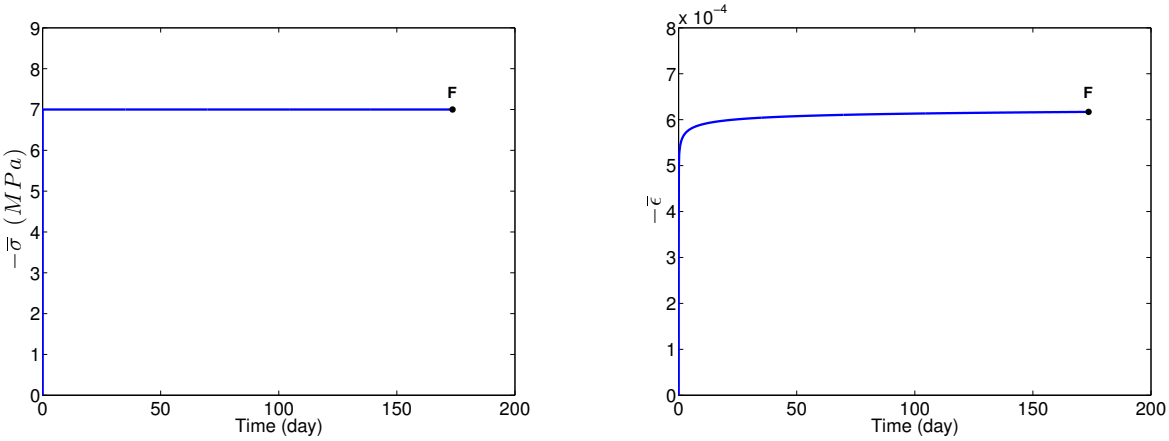

Figure 7: Asymptotic creep behavior predicted by the micro-macro model, in the absence of grain breakage. (a) Stress path. (b) Time evolution of macroscopic strains.

For each grain, the principal values of the micro-stress can be represented by a vector $\sigma_i \overrightarrow{v}_i$, where the unit vector $\overrightarrow{v}_i$ is the ith microstress eigenvector and σ_i is the ith microstress eigenvalue. In the plane (r, z), a tensile principal stress is represented by a vector $\overrightarrow{OM}$ (in the upper right quadrant, $z > 0$, $r > 0$), and a compressive principal stress is represented by a vector $\overrightarrow{ON}$ (in the lower left quadrant, $z < 0$, $r < 0$). The convention adopted to plot microscopic stresses is illustrated in Figure 8, in which α measures the angle between the direction of the principal microstress considered and the compression axis z. Stress maps drawn according to the convention explained in Figure 8 show the sign and amplitude of the principal microstresses, as well as the angle made by the principal microstresses with the compression axis, for each grain orientation considered in the REV.

Figure 9 illustrates the evolution of microscopic stresses at the beginning of both creep tests. Point A represents the state of stress in the aggregate after the first load has instantaneously been applied. Viscoplastic strains have not developed yet; therefore, the polycrystal follows a linear elastic behavior, and the microscopic stress in all grains is equal to the imposed macroscopic stress (7 MPa in the vertical direction, 0 MPa in the lateral directions). Microscopic gliding mechanisms result in a redistribution of micro-stresses, and, in particular, in a continuous increase of tensile microscopic stresses in the lateral directions (from A to B and from B to C). Microscopic stresses get closer and closer to the tensile limit of 2 MPa over time, which could explain the triggering of grain breakage for extended periods of time (note that grain breakage will be accounted for in the next section).

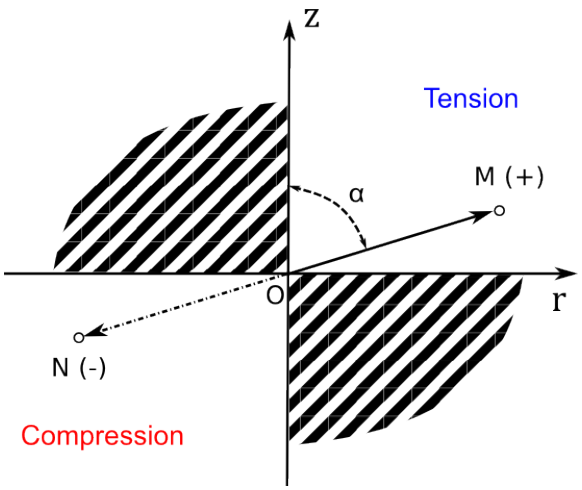

Figure 8: Graphical representation of the microscopic principal stresses.

The comparison of the distribution of microscopic stresses at points C (in Figure 9) and D (in Figure 10) provides a micro-mechanical explanation to the phenomenon of creep recovery. If the sample were instantaneously subjected to axial stress increase from 0MPa to 1MPa, lateral tensile microstresses would increase over time, starting from a state of microstress equal to that of the macrostress (the explanation of this physical phenomenon is the same as for the first loading stage of 7MPa presented in Figure 9). The response predicted when a creep load of 1MPa is applied after a creep load at 7MPa is very different from the one that would be expected without pre-loading phase: the distribution of microstresses tends to an isotropic distribution. A vertical tensile microstress of up to 1.3 MPa is noted in some of the grains, despite the applied macroscopic compressive stress, which amounts to 1MPa. The presence of vertical tensile microstresses within the aggregate explains why the specimen is in extension during this creep recovery stage (Figure 6). By contrast, Figure 11 shows that, if the first creep load of 7 MPa is maintained for extended periods of time (up to 180 days), tensile lateral microstresses will continue to increase at a slower rate (point E), and finally stabilize at an asymptotic value (point F). It is worth noticing that in in this simulation, the asymptotic value of the tensile microstresses exceeds the tensile strength (2MPa) in some of the grains, because grain breakage was not accounted for in the simulations (if it were accounted for, broken grains would undergo zero microstresses, which would appear in the form of a point at the origin of the plot).

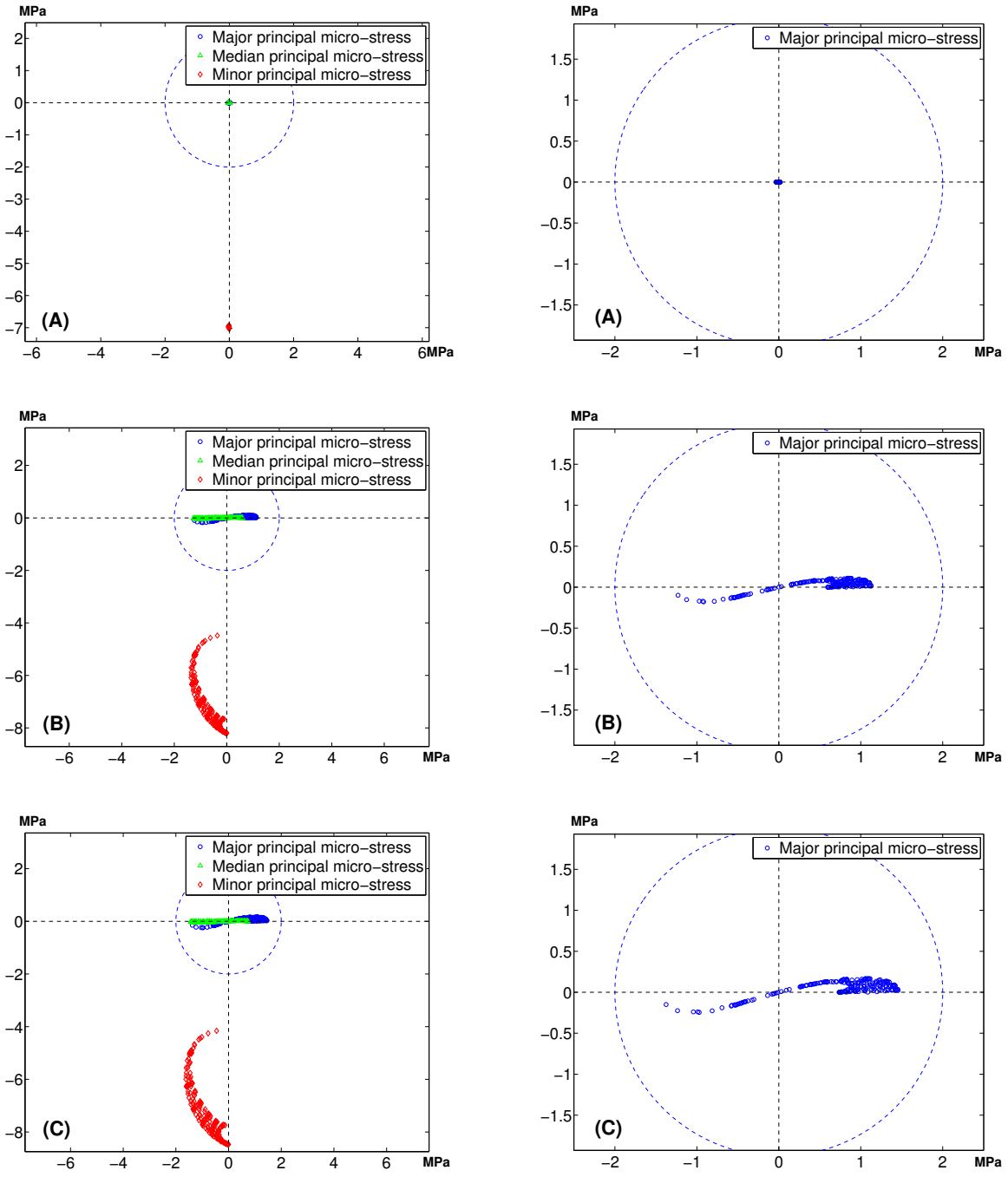

Figure 9: Micro-stress developed in the sample during the first stages of the two long-term creep tests simulated in the absence of grain breakage: loading points A, B, C shown in Figure 6.

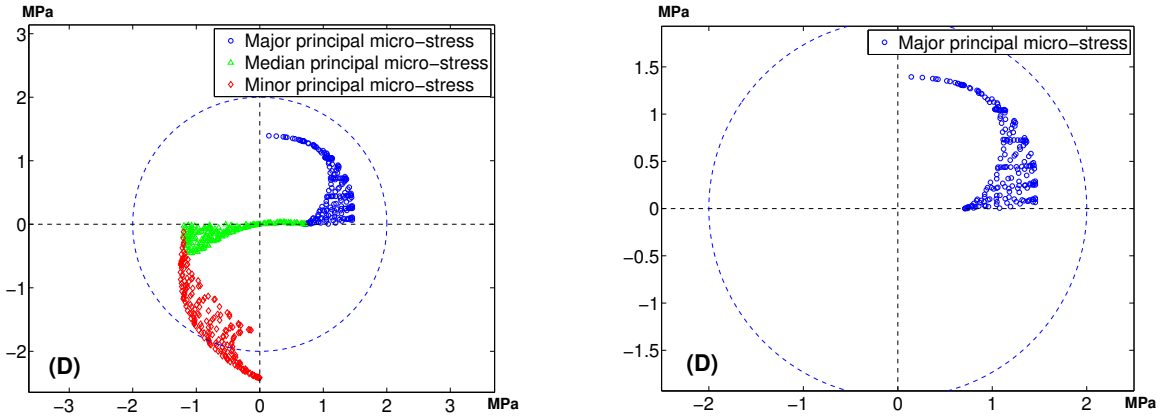

Figure 10: Micro-stress developed in the sample during the two-stage creep test simulated in the absence of grain breakage: loading point D shown in Figure 6.

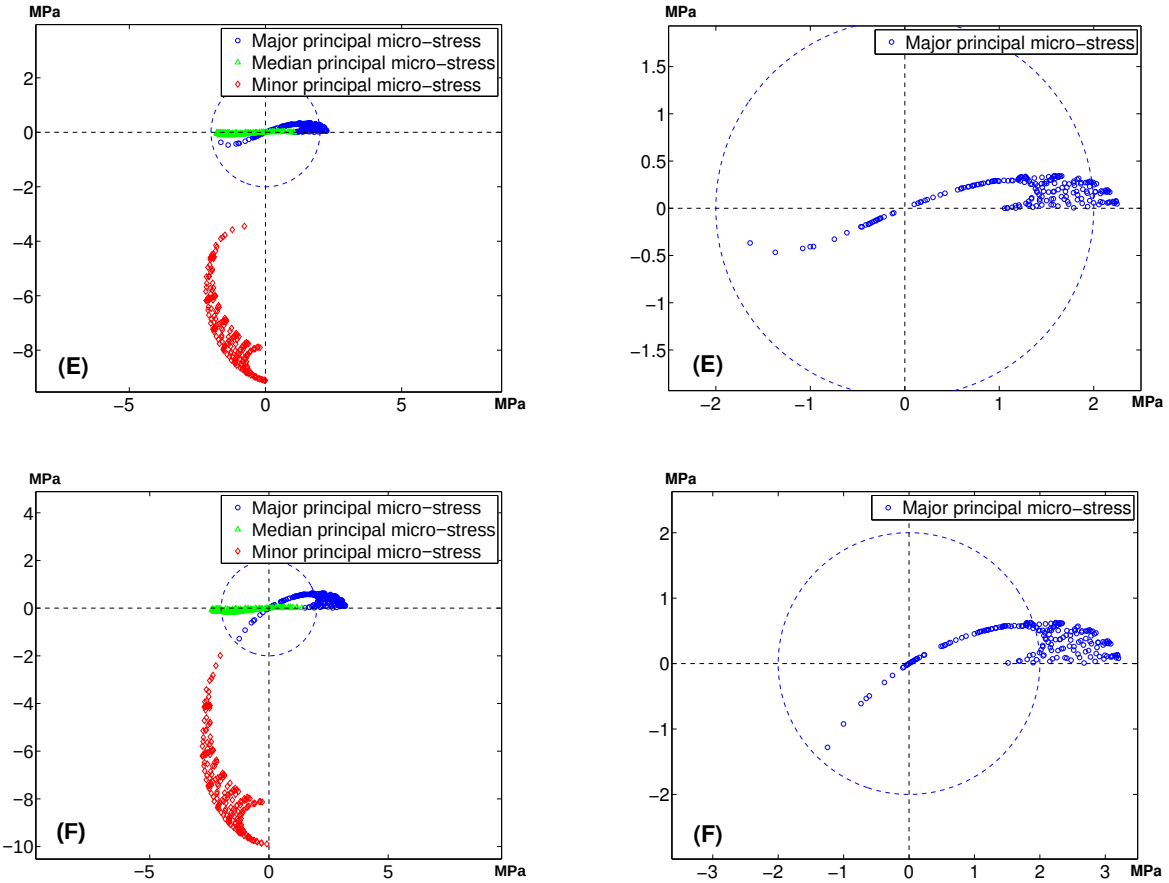

Figure 11: Micro-stress developed in the sample during the first creep test simulated in the absence of grain breakage: loading points E and F shown in Figures 6 and 7.

6.2. Influence of Grain Breakage

The three following long-term creep tests were simulated:

- In the first test ("no damage" case), a low creep stress (5 MPa) was applied, and grain breakage was accounted for.
- In the second test ("non-damage model" case), a higher creep stress (7 MPa) was applied, and grain breakage was not accounted for.
- In the third test ("damage model" case), a high creep stress (7 MPa) was applied, and grain breakage was accounted for.

The following model parameters were employed: $\gamma_0 = 2.93 \times 10^{-5}\,\mathrm{day}^{-1}$, $n = 4.04$. Results are presented in Figure 12:

- In the first test, the macroscopic strain rate reached almost a steady state typical of secondary creep, which indicates an absence of accelerated creep. Microscopic tensile stresses remained below 2 MPa, which implies that none of the mono crystals break, even though grain breakage was taken into account in the model.
- In the second test, the macroscopic strain rate remained in secondary creep, and microscopic stresses exceeded the tensile strength limit, which indicates that grains would have broken if damage had been accounted for.
- This last statement was confirmed by the third test, in which the microstress went to zero in some of the grains, and the macroscopic strain rate increased abruptly at the end of the creep test.

These results indicate that the model can capture the accelerated creep regime (tertiary creep) caused by grain breakage. The simulations reproduce well the trends observed in the experiments reported in [13] (Figures 4 and 5 in particular).

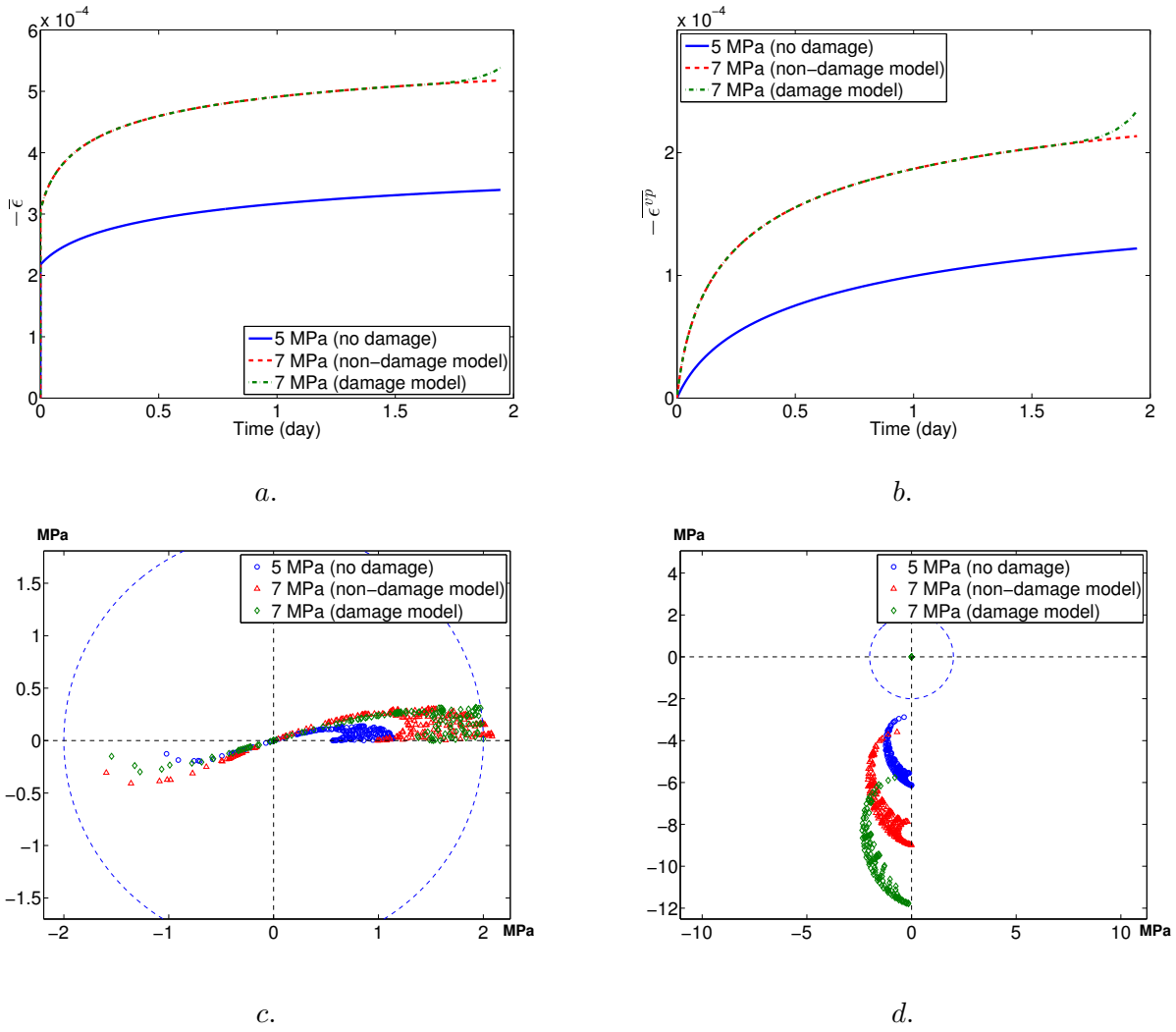

Figure 12: Comparison of different creep tests, with and without account for grain breakage. (a) Time evolution of total macrostrains. (b) Time evolution of viscoplastic macrostrains. (c) Major microstress component at the end of the creep tests. (d) Minor microstress component at the end of the creep tests.

7. Application: Salt Fatigue During Cyclic Loading

7.1. Damage Triggering due to Grain Viscous Deformation

The simulations presented in this subsection were performed with no account for grain breakage, in order to focus the discussion on the increase of microscopic stress leading to the initiation of damage due to grain breakage. The parameters calibrated for the long-term creep behavior were adopted: $\gamma_0 = 2.93 \times 10^{-5} day^{-1}$, $n = 4.04$.

7.1.1. Effect of the Loading Frequency

First, stress-controlled cyclic loading tests were simulated, for the sinusoidal loading given in Equation 30, with a maximum stress of 8 MPa and a loading amplitude of 2 MPa. Results after 15 cycles were compared for two frequencies typical of CAES conditions: 2 day^{-1} and 1 day^{-1} (Figure 13.a). In Equation 30, different frequencies result in different stress rates. In the absence of grain breakage, the macroscopic viscoplastic deformation is solely due to the microscopic viscoplastic strains that develop in the grains. Higher the frequency, higher the stress rate, shorter the time to develop viscoplastic strains. Therefore, for the same final macroscopic stress, higher frequencies will lead to smaller viscoplastic strains: this phenomenon is illustrated in Figures 13.b. and 13.d. Figure 13.c shows the resulting stress-strain curve, which is similar to the experimental curves reported in [13] (Figure 7 in particular). The stress-strain cycles tend to a limit behavior, with a constant shifting at each cycle. This limit behavior has some analogy with the "adaptation" or "shakedown" effect in elastoplastic media, in which the stress-strain curve exhibits a limit cycle after a large number of loading cycles. It has to be noted that the effect observed here for viscoplastic deformation is slightly different, because a constant residual cycle shift will remain, due to the non-zero average viscous deformation that develops during one cycle. The determination of the limit cycle could enable the prediction of the response expected after a high number of cycles, without modeling the transient effects of intermediate cycles. Figure 14 shows the distribution of internal stresses at the end of the loading tests, at the maximum stress. The results confirm that at higher frequency, less microscopic viscoplastic strains develop, which leads to smaller microscopic stresses. Note that the tensile microscopic stress exceeds the tensile strength of the mono-crystal in some of the grains, because grain breakage was not accounted for in the simulations.

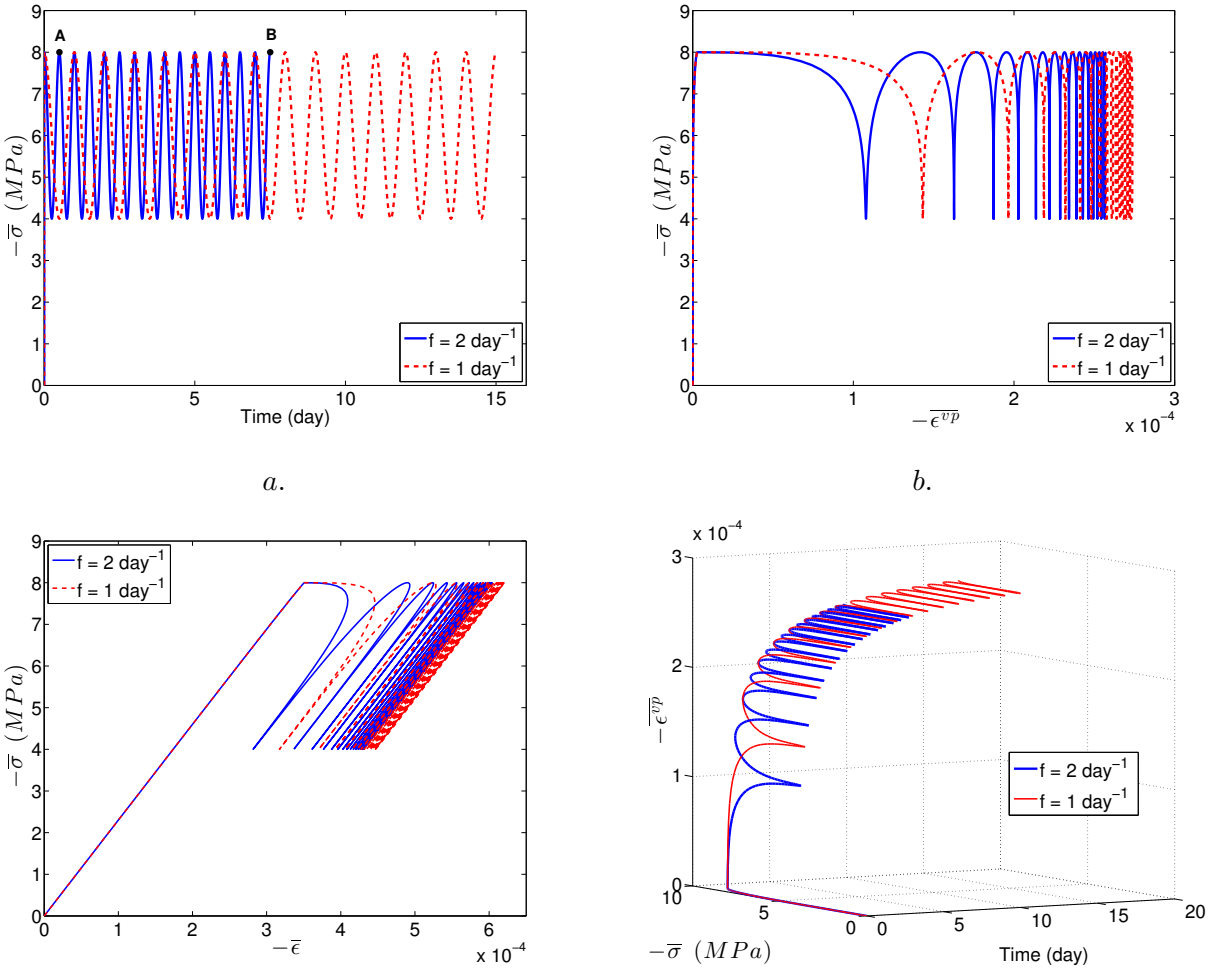

a. *b.* *c.* *d.*

Figure 13: Effect of the frequency of loading on macroscopic strains, in the absence of grain breakage. (a) Cyclic loading imposed in the simulation. (b) Evolution of macroscopic viscoplastic strains with macroscopic stress. (c) Macroscopic stress/strain curve. (d) Evolution of the macroscopic viscoplastic strain with macroscopic stress and time.

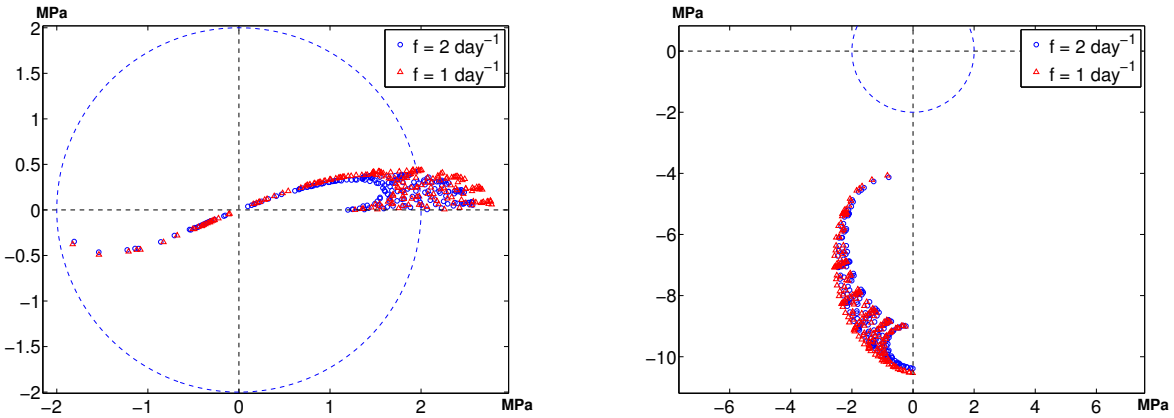

Figure 14: Internal stress distribution at the end of the cyclic loading test, for different loading frequencies, in the absence of grain breakage.

7.1.2. Effect of the Number of Cycles

For the cyclic loading test simulated at a frequency of 2 day^{-1}, the distribution of internal stresses at maximum stress after 15 cycles (point B in Figure 13.a) was compared to that after the first loading cycle (point A in Figure 13.a). As expected, microscopic stresses increase with the number of cycles: the tensile microstresses in the grains remain below the mono-crystal tensile strength after one cycle, and exceed the tensile limit after 15 cycles. Higher the number of cycles under the same loading frequency, longer the loading time, larger the microscopic viscoplastic strains, and higher the microstresses. In fact, the effect of the number of cycles is essentially an effect of time.

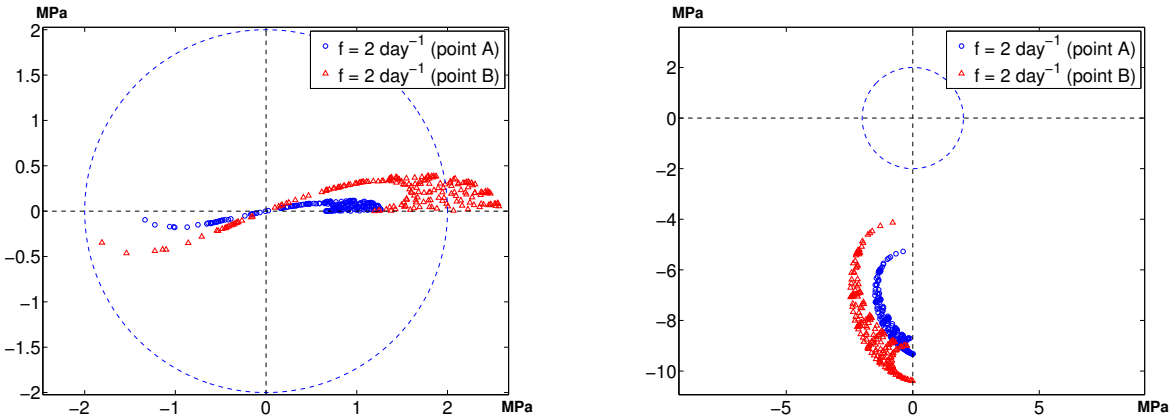

Figure 15: Internal stress distribution after 1 cycle (point A in Figure 13.a) and after 15 cycles (point B in Figure 13.a) during a cyclic loading applied with a frequency of 2 day^{-1}, in the absence of grain breakage.

7.2. Damage Propagation due to Grain Breakage

In the simulations presented in the following section, grain breakage was accounted for. The parameters calibrated for the long-term creep behavior were adopted: $\gamma_0 = 2.93 \times 10^{-5} day^{-1}$, $n = 4.04$. The response of the polycrystal to a sinusoidal cyclic loading of frequency 0.03 Hz (= 2592 day^{-1}) was studied for several maximum loading stresses and loading amplitudes. Two types of behaviors were observed:

- For small maximum stress and small loading amplitude, a limit cycle was reached. The number of broken grains (N_b) remained low, and Young's modulus decreased to a finite limit value. An example is shown in Figure 16, in which the maximum loading stress was 14 MPa and the amplitude was 6 MPa. Grain breakage first occurred at the 164^{th} cycle. The whole polycrystal failed after the 191^{th} cycle.

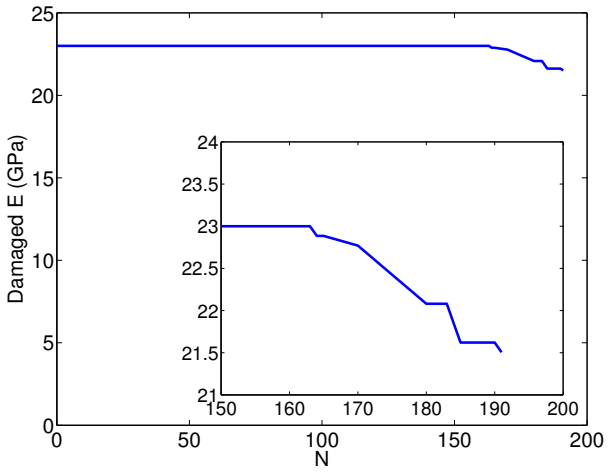

Figure 16: Evolution of the damaged Young's modulus with the number of cycles (f=0.03 Hz= 2592 day^{-1}; max. stress = 14 MPa; stress amplitude = 6 MPa).

- For larger maximum stress or larger loading amplitude, failure occurred after a limited number of cycles. Figure 17 shows the results obtained for a cyclic loading with a maximum loading stress of 20 MPa and an amplitude of 10 MPa. In the figure showing the minor principal microstresses, some grains experience zero stress, which indicates that they are broken. Grain breakage first occurred at the 6^{th} cycle, and the whole polycrystal failed after the 8^{th} cycle. The increasing number of broken grains is visible in the progressive reduction of the

Young's modulus in the plot showing the macroscopic stress/strain curve. These results are in agreement with the experimental results reported in Figure 7 of [13]. Damage initiates after a low number of cycles, and the behavior becomes extremely brittle thereafter: total failure usually occurs less than five cycles after the initiation of damage.

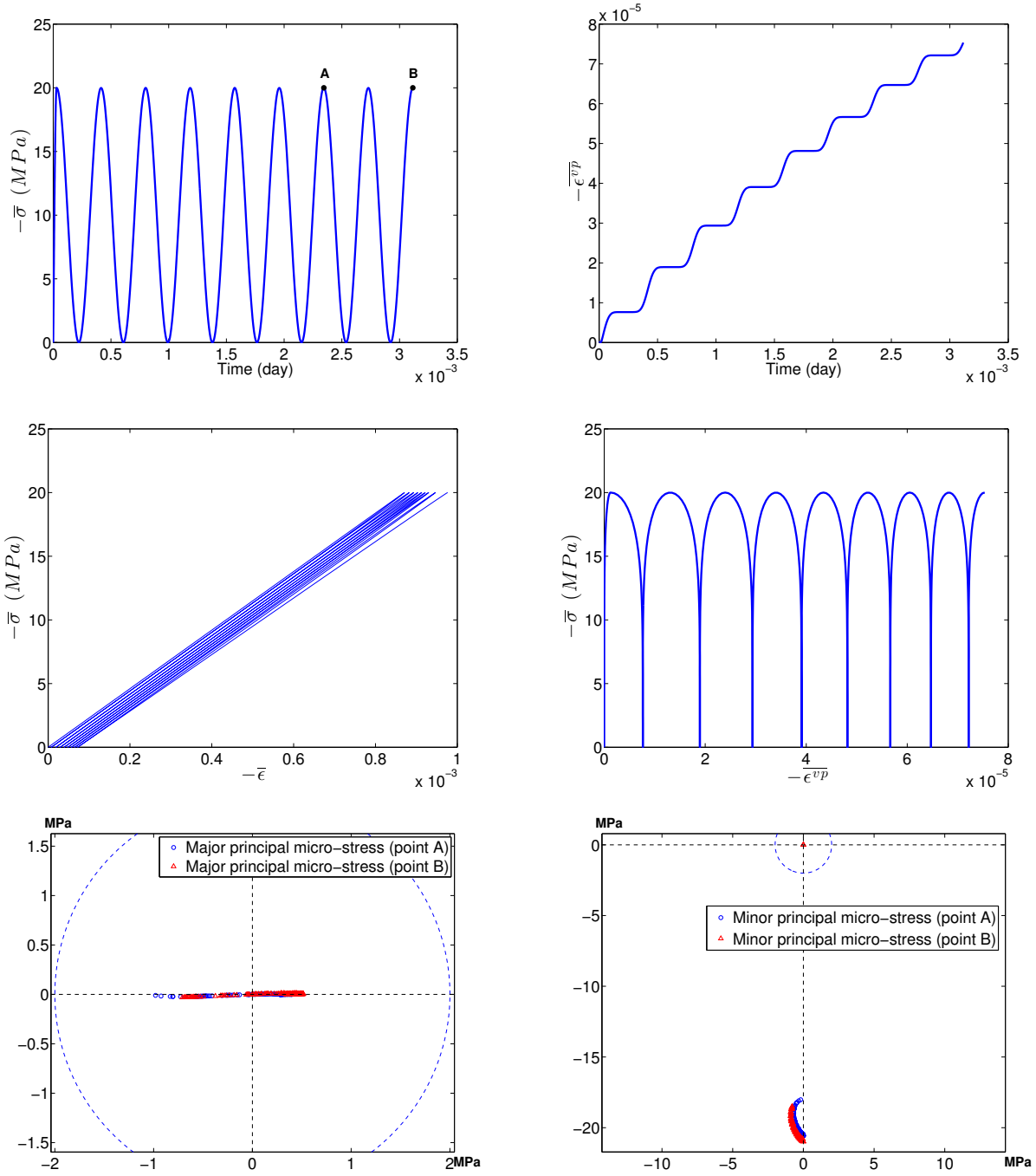

Figure 17: Simulation of a cyclic loading with a frequency of 0.03 Hz= 2592 day^{-1}, a maximum loading stress of 20 MPa and an amplitude of 10 MPa, with account for grain breakage. After 6 cycles, 2 grains are broken (point A). After 8 cycles, 7 grains are broken (point B).

8. Conclusion

In this paper, we formulated a micromechanical model of viscous fatigue for salt rock, which was considered as an aggregate of halite mono-crystals. The Representative Elementary Volume (REV) contained mono-crystals that have a uniform distribution of orientations. Viscoplastic strains at the grain scale were triggered by the activation of preferential gliding mechanisms, which were governed by a power law. We related microscopic stresses to macroscopic stress, macroscopic viscoplastic strains and microscopic viscoplastic strains, by means of an inclusion-matrix model. We extended a self-consistent homogenization scheme, initially proposed for elasto-plasticity, to viscoplasticity. We introduced a grain breakage condition, which allowed predicting the progressive loss of stiffness and strength of the aggregate upon cyclic loading. Damage was defined as the ratio of the number of broken grains by the total number of grain orientations considered in the REV.

Although simplifying assumptions were made to represent the shape and behavior of the mono-crystals, the micro-mechanical modeling approach enabled predicting important aspects of salt rock viscoplastic and damage behavior. Strain hardening during creep was evidenced by the increase of macroscopic viscoplastic strains at a decreasing rate, and by the progressive increase of microscopic stresses over time, until an asymptotic value. In creep tests in which a high compressive stress was applied before a lower compressive stress, tensile macroscopic strains were accompanied by a re-orientation of microscopic stresses towards an isotropic distribution: simulations provided a microscopic interpretation to the phenomenon known as "creep recovery", which is a memory effect. Grain breakage occurred for creep tests under high stress, and for cyclic loading tests simulated at lower frequencies, higher maximum stress, and/or higher loading amplitude. As expected, the Young's modulus decreased with the increase of damage. Grain breakage provided a micro mechanical explanation to the phenomenon known as "accelerated creep" (also called "tertiary creep"). The dependence of viscoplastic strains to cyclic loading frequency was well captured by the model: higher the frequency, smaller the macroscopic viscoplastic strain, and smaller the microscopic stresses. The increment of macroscopic viscoplastic deformation decreased over the cycles, which is in agreement with the phenomenon of plastic adaptation or "shakedown" observed in elasto-plastic media.

The study of this "adaptation" effect was beyond the scope of this paper. However, the determination of limit cycles would open interesting perspectives for the modeling the long term

behavior of, for instance, salt caverns under cyclic loading. More work is needed to account for non-elastic inclusion/matrix interactions known as "viscous accommodation", which results from geometric incompatibilities between grains. The damage model could also be improved in order to account for the residual stiffness of grains broken into several parts, instead of considering that broken grains behave like holes in the matrix. This aspect of damage modeling requires introducing elastic anisotropy in the model, for both the grains and the matrix. Theoretical and numerical developments are currently underway to account for the development of frictional discontinuities between grains in time-dependent loading conditions.

Appendix A. Experimental studies of salt fatigue under cyclic loading

Table A.3: Review of experimental studies of salt fatigue under cyclic loading.

Salt studied	Loading conditions (σ_{max} = maximum stress; σ_{min} = minmum stress; N = Number of cycles; f = frequency; $\dot{\varepsilon}$ = strain rate)	Key findings	Reference
78.84% NaCl, 18.92% water insoluble materials (quartz, clay, mud, and marl), 2.14-2.74% $MgCl_2$ and $CaSO_4$ (India)	σ_{max} = 10, 20, 30, 40, 50, 60, 65, 70, 72, 75% of the compressive strength; $f = 3.5 \times 10^{-3}$ Hz; N = 50-400	Below a certain stress level, the compressive strength and the elastic modulus depend on intrinsic anisotropy (bedding plane) and on the number of cycles; above this stress level, the influence is negligible.	Dubey and Gairola, 2000 [52]
pure rock salt and less than 0.5% insoluble component (Russia)	N = 2: triaxial compression followed by uniaxial compression	Memory effects in stress were measured when the maximum in-situ stress exceeded the elastic limit.	Filimonov et al., 2001 [57]
relatively pure halite with less than 1-2% anhydrite, clay minerals and ferrous oxide (Thailand)	σ_{max} = 15.9 to 34.6 MPa; σ_{max} = 0.15 MPa; $f = 0.001 - 0.3$ Hz; N = 7-595	Strength decreases for larger numbers of loading cycles; salt visco-plasticity decreases with increasing loading frequency.	Fuenkajorn and Phueakphum, 2010 [13]
two types of samples: salt rock with pure halite; salt rock dominated by thenardite (Na_2SO_4) (China)	uniaxial compression; $\dot{\varepsilon}$ = 2×10^{-5}, 2×10^{-4}, $2 \times 10^{-3} s^{-1}$; σ_{max} = 12.5-15.4 MPa	Elastic moduli slightly increase with the strain rate; Poisson's ratio decreases with the strain rate; the failure stress is lower for lower strain rates.	Liang et al., 2011 [54]
high purity (NaCl, Na_2SO_4, $CaSO_4$) with less than 10% insolubles (glauberite, argillaceous, anhydrite) (China)	σ_{max} = 75-90% of the compressive strength; σ_{min} = 37.5-45% of the compressive strength; f = 1 Hz; N =1041-14789	The maximum and mean stresses affect fatigue significantly; failure modes for uniaxial compression and cyclic loading are different.	Guo et al., 2012 [56]
75-85% NaCl (halite), 0.72% Na_2SO_4 (sodium sulfate), 1.2% $CaSO_4$ (anhydrite), 7-10% insoluble components (China)	σ_{max} = 24.9-53.2 MPa; σ_{min} = 16.9-28.2 MPa; sinusoidal form; $f = 0.025, 0.05, 0.1$ Hz; confining pressure = 7, 14, 21 MPa; N =500-850	Elastic moduli decrease exponentially for increasing number of cycles; modulus degradation is independent of stress level and confining pressure; higher loading frequencies cause less viscoplastic deformation; triaxial compressive strength and total strain increase with stress amplitude, loading frequency, and confining pressure.	Ma et al., 2013 [53]
salt rock with salt content up to 84.76-93.76% (China)	σ_{max} = 20, 30, 40, 50, 60, 70, 85% of the compressive strength (20 MPa); σ_{min} = 1 MPa; sinusoidal form; f = 1 Hz; N = 31	The stress level leading to the initiation of fatigue damage under cyclic loading is 20% of the uniaxial compressive strength; damage accumulation accelerates beyond the point of volume expansion.	Liu et al., 2014 [55]

Appendix B. Expression of gliding mechanisms in the global coordinate system

In the global coordinate system, the l^{th} gliding mechanism $\left[\mathbf{a}^l\right]$ can be related to that in the local coordinate system, $\left[\mathbf{A}^l\right]$ (given by Equation 1), by means of a projection tensor $[\mathbf{P}]$ which depends on the orientation of the mono crystal:

$$\left[\mathbf{a}^l\right] = [\mathbf{P}] \left[\mathbf{A}^l\right] [\mathbf{P}]^T \tag{B.1}$$

The projection tensor $[\mathbf{P}]$ is decomposed as $[\mathbf{P}] = [\mathbf{P}_1][\mathbf{P}_2][\mathbf{P}_3]$, with:

$$[\mathbf{P_1}] = \begin{bmatrix} cos\Psi & sin\Psi & 0 \\ -sin\Psi & cos\Psi & 0 \\ 0 & 0 & 1 \end{bmatrix} \quad [\mathbf{P_2}] = \begin{bmatrix} cos\theta & 0 & sin\theta \\ 0 & 1 & 0 \\ -sin\theta & 0 & cos\theta \end{bmatrix} \quad [\mathbf{P_3}] = \begin{bmatrix} cos\Phi & -sin\Phi & 0 \\ sin\Phi & cos\Phi & 0 \\ 0 & 0 & 1 \end{bmatrix} \tag{B.2}$$

Ψ, θ, and Φ are the angles giving the orientation of the grain as described in Section 3.1.

Appendix C. Kröner-Weng model

For a homogeneous and isotropic elastic matrix, Kröner's model [44], proposed initially for elasto-plastic materials, was extended by Weng for viscoplastic materials [45], in the following form:

$$\dot{\boldsymbol{\sigma}} - \dot{\overline{\boldsymbol{\sigma}}} = 2\mu(1-\beta)(\dot{\overline{\boldsymbol{\varepsilon}}}^{vp} - \dot{\boldsymbol{\varepsilon}}^{vp}) \tag{C.1}$$

In which $\dot{\boldsymbol{\sigma}}$ is the rate of microscopic stress, and $\dot{\overline{\boldsymbol{\sigma}}}$ is the rate of macroscopic stress. $\dot{\overline{\boldsymbol{\varepsilon}}}^{vp}$ and $\dot{\boldsymbol{\varepsilon}}^{vp}$ denote the macroscopic and microscopic viscoplastic strain rates. β is given by:

$$\beta = \frac{2(4-5\nu)}{15(1-\nu)} \tag{C.2}$$

In which ν is the Poisson's ratio of both the matrix and the grains (uniform elasticity). According to equation 6, the microscopic and macroscopic viscoplastic strains are purely deviatoric. Taking the deviatoric part of equation C.1 yields:

$$\dot{\mathbf{s}} = \dot{\overline{\mathbf{s}}} + 2\mu(1-\beta)(\dot{\overline{\boldsymbol{\varepsilon}}}^{vp} - \dot{\boldsymbol{\varepsilon}}^{vp}) \tag{C.3}$$

Where $\mathbf{s}$ and $\overline{\mathbf{s}}$ are the micro- and macro- deviatoric stresses, respectively.

Appendix D. Approximated macroscopic visco-plastic law

We derive a simple relationship between the macroscopic viscoplastic strain rate and the macroscopic stress imposed during the simulations. Let us recall the constitutive law adopted in the model:

$$\dot{\boldsymbol{\varepsilon}}^{vp} = \sum_{l=1}^{6} \dot{\gamma}^l \boldsymbol{a}^l, \quad \dot{\gamma}^l = \gamma_0 \, h^l \left| \frac{\tau^l}{\tau_0} \right|^n, \quad \tau^l = \boldsymbol{\sigma} : \mathbf{a}^l \tag{D.1}$$

And the homogenization scheme based on Weng's model (equation C.3), for the axial loading (equations 27-28), provides:

$$\dot{\mathbf{s}} = \dot{\rho(t)} \boldsymbol{\Psi} - 2\mu(1-\beta)\dot{\boldsymbol{\varepsilon}}^{vp} \tag{D.2}$$

Taking the average of Equation D.2:

$$\dot{\bar{\mathbf{s}}} = \dot{\rho}(t)\boldsymbol{\Psi} - 2\mu(1-\beta)\langle\dot{\boldsymbol{\varepsilon}}^{vp}\rangle \tag{D.3}$$

We propose to approximate the relation given in Equation D.2 by replacing the microscopic stress $\boldsymbol{\sigma}$ by the macroscopic stress $\overline{\boldsymbol{\sigma}} = q(t)\mathbf{r}$ in expression D.1. Equation D.3 then becomes:

$$\dot{q}(t)\boldsymbol{\Psi} = \dot{\rho}(t)\boldsymbol{\Psi} - 2\mu(1-\beta)\langle\sum_{l=1}^{L} \gamma_0 \, h^l \left| \frac{q(t)\mathbf{r} : \mathbf{a}^l}{\tau_0} \right|^n \mathbf{a}^l\rangle \tag{D.4}$$

Multiplying both sides of equation D.4 by $\boldsymbol{\Psi}$:

$$\dot{q}(t)\boldsymbol{\Psi} : \boldsymbol{\Psi} = \dot{\rho}(t)\boldsymbol{\Psi} : \boldsymbol{\Psi} - 2\mu(1-\beta)\langle\sum_{l=1}^{L} \gamma_0 \, h^l \left| \frac{q(t)\mathbf{r} : \mathbf{a}^l}{\tau_0} \right|^n \mathbf{a}^l : \boldsymbol{\Psi}\rangle \tag{D.5}$$

Then noticing that $Tr(\mathbf{a}^l) = 0$, Equation D.5 can be rewritten as:

$$\dot{q}(t)\boldsymbol{\Psi} : \boldsymbol{\Psi} = \dot{\rho}(t)\boldsymbol{\Psi} : \boldsymbol{\Psi} - 2\mu(1-\beta)\langle\sum_{l=1}^{L} \gamma_0 \, h^l \left| \frac{q(t)\mathbf{r} : \mathbf{a}^l}{\tau_0} \right|^n \boldsymbol{r} : \mathbf{a}^l\rangle \tag{D.6}$$

Noticing that $h^l \cdot \mathbf{r} : \mathbf{a}^l$ has the same sign as $\tau^l \cdot \mathbf{r} : \mathbf{a}^l$, and since $q(t) \geq 0$, we have:

$$\tau^l \cdot \mathbf{r} : \mathbf{a}^l = (\overline{\boldsymbol{\sigma}} : \mathbf{a}^l) \cdot (\mathbf{r} : \mathbf{a}^l) = q(t) \cdot (\mathbf{r} : \mathbf{a}^l) \cdot (\mathbf{r} : \mathbf{a}^l) \geq 0 \tag{D.7}$$

Therefore:

$$h^l \cdot \mathbf{r} : \mathbf{a}^l = |\mathbf{r} : \mathbf{a}^l| \tag{D.8}$$

Equation D.6 can be rewritten as:

$$\dot{q}(t)\boldsymbol{\Psi} : \boldsymbol{\Psi} = \dot{\rho}(t)\boldsymbol{\Psi} : \boldsymbol{\Psi} - 2\mu(1-\beta)\langle\sum_{l=1}^{L} \gamma_0 \left| \frac{q(t)}{\tau_0} \right|^n \left| \mathbf{r} : \mathbf{a}^l \right|^{n+1}\rangle \tag{D.9}$$

After dividing by $(\mathbf{\Psi} : \mathbf{\Psi})$:

$$\dot{q}(t) \;=\; \dot{\rho}(t) - \; q^n(t)\,\frac{1}{(\tau_0)^n}\,\frac{2\mu(1-\beta)}{\mathbf{\Psi} : \mathbf{\Psi}}\langle\sum_{l=1}^{L}\gamma_0\,\left|\mathbf{r} : \mathbf{a}^l\right|^{n+1}\rangle \tag{D.10}$$

Then recalling that $(\mathbf{\Psi} : \mathbf{\Psi}) = 2/3$, Equation D.10 can be simplified into:

$$\dot{q}(t) \;=\; \dot{\rho}(t) - \; \frac{q^n(t)}{(\tau_0)^n}\,\underbrace{3\mu(1-\beta)\langle\sum_{l=1}^{L}\gamma_0\,\left|\mathbf{r} : \mathbf{a}^l\right|^{n+1}\rangle}_{M} \tag{D.11}$$

The expression of q as a function of time is obtained by solving the following non-linear differential equation:

$$\dot{q}(t) \;+\; M\,\frac{q^n(t)}{(\tau_0)^n} \;=\; \dot{\rho}(t) \tag{D.12}$$

Recalling that:

$$\dot{\rho}(t) = \dot{q}(t) + 3\mu(1-\beta)\dot{p}(t) \tag{D.13}$$

The following equation is obtained:

$$\dot{p}(t) \;=\; \frac{M}{3\mu(1-\beta)}\,\frac{q^n(t)}{(\tau_0)^n} \tag{D.14}$$

Equation D.14, based on an approximation, provides a direct relationship between the macroscopic viscoplasic strain rate $\dot{p}(t)$ and the macroscopic stress $q(t)$.

References

[1] D. E. Munson, Preliminary deformation-mechanism map for salt (with application to wipp), Tech. rep., Sandia Labs., Albuquerque, NM (USA) (1979).

[2] D. Munson, P. Dawson, Constitutive model for the low temperature creep of salt (with application to wipp), Tech. rep., Sandia Labs., Albuquerque, NM (USA) (1979).

[3] M. Langer, The rheological behavior of rock salt, in: Proc. First Conf. Mech. Behavior of Salt, Trans Tech Publications, Germany, 1981, pp. 201–240.

[4] M. Ghoreychi, Mechanical behavior of salt: 3rd conference, Ecole Polytechnique, Palaiseau, France, September 14-16, 1993, Vol. 20, Trans Tech Pubn, 1996.

[5] K. Chan, S. Bodner, A. Fossum, D. Munson, A damage mechanics treatment of creep failure in rock salt, International Journal of Damage Mechanics 6 (2) (1997) 121–152.

[6] U. Hunsche, A. Hampel, Rock salt — the mechanical properties of the host rock material for a radioactive waste repository, Engineering geology 52 (3) (1999) 271–291.

[7] F. Chen, Y. Li, C. Yang, C. Zhang, Experimental study on creep behaviors of rock salt in yunying salt mine., Yanshilixue Yu Gongcheng Xuebao/Chinese Journal of Rock Mechanics and Engineering 25 (2006) 3022–3027.

[8] M. L. Jeremic, Rock mechanics in salt mining, CRC Press, 1994.

[9] W.-g. Liang, C.-h. Yang, Y.-s. Zhao, M. Dusseault, J. Liu, Experimental investigation of mechanical properties of bedded salt rock, International Journal of Rock Mechanics and Mining Sciences 44 (3) (2007) 400–411.

[10] K. Staudtmeister, R. Rokahr, Rock mechanical design of storage caverns for natural gas in rock salt mass, International Journal of Rock Mechanics and Mining Sciences 34 (3) (1997) 300–e1.

[11] P. Bérest, J. Bergues, B. Brouard, J. Durup, B. Guerber, A salt cavern abandonment test, International Journal of Rock Mechanics and Mining Sciences 38 (3) (2001) 357–368.

[12] W. Wu, Z.-m. Hou, C.-h. Yang, Investigations on evaluating criteria of stabilities for energy (petroleum and natural gas) storage caverns in rock salt, Chinese Journal of Rock Mechanics and Engineering 24 (14) (2005) 2497–2505.

[13] K. Fuenkajorn, D. Phueakphum, Effects of cyclic loading on mechanical properties of maha sarakham salt, Engineering Geology 112 (1) (2010) 43–52.

[14] R. Stokes, Mechanical properties of polycrystalline sodium chloride, Brit. Ceram. Soc. Proc. 6 (1966) 187–207.

[15] N. L. Carter, H. C. Heard, Temperature and rate dependent deformation of halite, American Journal of Science 269 (3) (1970) 193–249.

[16] N. L. Carter, F. D. Hansen, Creep of rock salt, Tectonophysics 92 (4) (1983) 275–333.

[17] J. L. Urai, C. J. Spiers, H. J. Zwart, G. S. Lister, Weakening of rock salt by water during long-term creep, Nature 324 (1986) 554–557.

[18] P. Senseny, F. Hansen, J. Russell, N. Carter, J. Handin, Mechanical behaviour of rock salt: phenomenology and micromechanisms, International journal of rock mechanics and mining sciences & geomechanics abstracts 29 (4) (1992) 363–378.

[19] L. jian Ma, X. yu Liu, M. yang Wang, H. fa Xu, R. ping Hua, P. xian Fan, S. rong Jiang, G. an Wang, Q. kang Yi,

Experimental investigation of the mechanical properties of rock salt under triaxial cyclic loading, International Journal of Rock Mechanics and Mining Sciences 62 (2013) 34 – 41.

[20] C. Zhu, C. Arson, A model of damage and healing coupling halite thermo-mechanical behavior to microstructure evolution, Geotechnical and Geological Engineering 33 (2) (2014) 389–410.

[21] L. M. Taylor, E.-P. Chen, J. S. Kuszmaul, Microcrack-induced damage accumulation in brittle rock under dynamic loading, Computer Methods in Applied Mechanics and Engineering 55 (3) (1986) 301 – 320.

[22] E. Lajtai, E. Duncan, B. Carter, The effect of strain rate on rock strength, Rock Mechanics and Rock Engineering 24 (2) (1991) 99–109.

[23] S. Ray, M. Sarkar, S. TN, Effect of loading and strain rate on the mechanical behaviour of sandstone, International Journal of Rock Mechanics and Mining Sciences 36 (1999) 543–549.

[24] G. Prost, Jointing at rock contacts in cyclic loading, International Journal of Rock Mechanics and Mining Sciences & Geomechanics Abstracts 25 (5) (1988) 263 – 272.

[25] T. Z.Y., H. Mo, An experimental study and analysis of the behavior of rock under cyclic loading, International Journal of Rock Mechanics and Mining Sciences 27 (1) (1990) 51–56.

[26] X. J.Q., D. Ding, F. Jiang, X. G., Fatigue damage variable and evolution of rock subjected to cyclic loading, International Journal of Rock Mechanics and Mining Sciences 47 (2010) 461–468.

[27] P. Attewell, I. Farmer, Fatigue behaviour of rock, International Journal of Rock Mechanics and Mining Sciences & Geomechanics Abstracts 10 (1) (1973) 1 – 9.

[28] S. Singh, Fatigue and strain hardening behaviour of graywacke from the flagstaff formation, new south wales, Engineering Geology 26 (2) (1989) 171 – 179.

[29] M. Bagde, V. Petroš, Fatigue properties of intact sandstone samples subjected to dynamic uniaxial cyclical loading, International Journal of Rock Mechanics and Mining Sciences 42 (2) (2005) 237 – 250.

[30] M. Jafari, M. Boulon, K. Hosseini, Experimental study of mechanical behaviour of rock joints under cyclic loading, Rock Mechanics and Rock Engineering 37 (1) (2004) 3–23.

[31] N. Li, P. Zhang, C. Y.S., S. G., Fatigue properties of cracked, saturated and frozen sandstone samples under cyclic loading, International Journal of Rock Mechanics and Mining Sciences 40 (2003) 145–150.

[32] N. Burdine, Rock failure under dynamic loading conditions, Society of Petroleum Engineers 3 (1) (1963) 1–8.

[33] Y. Ishizuka, T. Abe, J. Kodama, Fatigue behavior of granite under cyclic loading, in: R. Brumer (Ed.), ISRM International Symposium - static and dynamic considerations in rock engineering, 1990, pp. 139–146.

[34] R. Mahnken, M. Kohlmeier, Finite element simulation for rock salt with dilatancy boundary coupled to fluid permeation, Computer Methods in Applied Mechanics and Engineering 190 (32–33) (2001) 4259 – 4278.

[35] L. J. Ladani, A. Dasgupta, A meso-scale damage evolution model for cyclic fatigue of viscoplastic materials, International Journal of Fatigue 31 (4) (2009) 703–711.

[36] B. Balendran, S. Nemat-Nasser, Double sliding model for cyclic deformation of granular materials, including dilatancy effects, Journal of the Mechanics and Physics of Solids 41 (3) (1993) 573–612.

[37] H. Mirkhani, S. Joshi, Mechanism-based crystal plasticity modeling of twin boundary migration in nanotwinned face-centered-cubicmetals, Journal of the Mechanics and Physics of Solids 68 (2014) 107133.

[38] C. Arson, H. Xu, F. Chester, On the definition of damage in time-dependent healing models for salt rock,

Géotechnique Letters 2 (April-June) (2012) 67–71.

[39] A. Pouya, Comportement rheologique du sel gemme application a l'etude des excavations souterraines, Ph.D. thesis, Ecole Nationale des Ponts et Chaussées, Paris (Oct. 1991).

[40] A. Pouya, Micro-macro approach for the rock salt behaviour, Eur. J. Mech. A/Solids 19 (2000) 1015–1028.

[41] A. Pouya, C. Zhu, C. Arson, Micro-macro modeling approach for the triggering of viscous fatigue damage in halite polycrystals under cyclic loading, in: 48th US Rock Mechanics/Geomechanics Symposium of the American Rock Mechanics Association, Minneapolis, MN, 1-4 June 2014, 2014, pp. paper ID: 14–6949.

[42] C. Zhu, C. Arson, A. Pouya, Theoretical and numerical matrix-inclusion models of damage accommodation in salt subject to viscous fatigue, in: Mechanical Behavior of Salt VIII, Rapid City, South Dakota, 26-28 May 2015, 2015.

[43] R. Hill, Continuum micro-mechanics of elastoplastic polycrystals, Journal of the Mechanics and Physics of Solids 13 (2) (1965) 89–101.

[44] E. Kröner, Zur plastischen verformung des vielkristalls, Acta metallurgica 9 (2) (1961) 155–161.

[45] G. Weng, A unified self-consistent theory for the plastic-creep deformation of metals, J. Appl. Mech 49 (1982) 728–734.

[46] Y. Rougier, C. Stolz, A. Zaoui, Self-consistent modelling of elastic-viscoplastic polycrystals, C.R. Acad. Sci. Paris, série II 318 (1994) 145–151.

[47] S. Mercier, A. Molinari, Homogenization of elastic–viscoplastic heterogeneous materials: Self-consistent and mori-tanaka schemes, International Journal of Plasticity 25 (6) (2009) 1024–1048.

[48] R. Masson, A. Zaoui, Self-consistent estimates for the rate-dependentelastoplastic behaviour of polycrystalline materials, Journal of the Mechanics and Physics of Solids 47 (7) (1999) 1543–1568.

[49] R. Masson, M. Bornert, P. Suquet, A. Zaoui, An affine formulation for the prediction of the effective properties of nonlinear composites and polycrystals, Journal of the Mechanics and Physics of Solids 48 (6) (2000) 1203–1227.

[50] M. Bornert, R. Masson, P. P. Castañeda, A. Zaoui, Second-order estimates for the effective behaviour of viscoplastic polycrystalline materials, Journal of the Mechanics and Physics of Solids 49 (11) (2001) 2737–2764.

[51] M. V. Nebozhyn, P. Gilormini, P. Ponte Castañeda, Variational self-consistent estimates for cubic viscoplastic polycrystals: the effects of grain anisotropy and shape, Journal of the Mechanics and Physics of Solids 49 (2) (2001) 313–340.

[52] R. Dubey, V. Gairola, Influence of structural anisotropy on the uniaxial compressive strength of pre-fatigued rocksalt from himachal pradesh, india, International Journal of Rock Mechanics and Mining Sciences 37 (2000) 993–999.

[53] J. Ma, L. X.Y., W. M.Y., H. Xu, R. Hua, F. P.X., J. S.R., W. G.A., Q. Yi, Experimental investigation of the mechanical properties of rock salt under triaxial cyclic loading, International Journal of Rock Mechanics and Mining Sciences 62 (2013) 34–41.

[54] W. Liang, Y. Zhao, S. Xu, M. Dusseault, Effect of strain rate on the mechanical properties of salt rock, International Journal of Rock Mechanics and Mining Sciences 48 (2011) 161–167.

[55] J. Liu, H. Xie, Z. Hou, C. Yang, C. L., Damage evolution of rock salt under cyclic loading in uniaxial tests, Acta Geotechnica 9 (2014) 153–160.

[56] G. Y.T., Y. C.H., M. H.J., Mechanical properties of jintan mine rock salt under complex stress paths, International Journal of Rock Mechanics and Mining Sciences 56 (2012) 54–61.

[57] Y. Filimonov, A. Lavrov, Y. Shafarenko, V. Shkuratnik, Memory effects in rock salt under triaxial stress state and their use for stress measurement in a rock mass, Rock Mechanics and Rock Engineering 34 (4) (2001) 275–291.

[58] H.-R. Wenk, A voyage through the deformed earth with the self-consistent model, Modelling and Simulation in Materials Science and Engineering 7 (5) (1999) 699.

[59] R. A. Lebensohn, P. R. Dawson, H. M. Kern, H.-R. Wenk, Heterogeneous deformation and texture development in halite polycrystals: comparison of different modeling approaches and experimental data, Tectonophysics 370 (1) (2003) 287–311.

[60] G. Groves, A. Kelly, Independent slip systems in crystals, Philosophical Magazine 8 (89) (1963) 877–887.

[61] A. Argon, A. Nigam, G. Padawer, Plastic deformation and strain hardening in pure nacl at low temperatures, Philosophical Magazine 25 (5) (1972) 1095–1118.

[62] R. Davidge, P. Pratt, Plastic deformation and work-hardening in nacl, physica status solidi (b) 6 (3) (1964) 759–776.

[63] W. Skrotzki, P. Haasen, The role of cross slip in the steady state creep of salt, in: second conference on the mechanical behavior of salt September, 1984, pp. 24–28.

[64] P. H. Wanten, C. J. Spiers, C. J. Peach, Deformation of nacl single crystals at 0.27 tm, Series on rock and soil mechanics 20 (1996) 117–128.

[65] A. Pouya, Correlation between mechanical behaviour and petrological properties of rock salt, in: The 32nd US Symposium on Rock Mechanics (USRMS), 1991, pp. 385–392.

[66] S. Nemat-Nasser, M. Hori, Micromechanics: overall properties of heterogeneous solids, Applied Mathematics and Mechanics. Elsevier, Amsterdam.

[67] J. G. Berryman, Mixture theories for rock properties, Rock Physics & Phase Relations: A Handbook of Physical Constants (1995) 205–228.

[68] B. Pichler, C. Hellmich, Upscaling quasi-brittle strength of cement paste and mortar: A multi-scale engineering mechanics model, Cement and Concrete Research 41 (2011) 467–476.

[69] A. Fritsch, C. Hellmich, P. Young, Micromechanics-derived scaling relations for poroelasticity and strength of brittle porous polycrystals, Journal of Applied Mechanics 80 (2) (2013) 1–12.

[70] M. Ortiz, A constitutive theory for the inelastic behavior of concrete, Mechanics of materials 4 (1) (1985) 67–93.

[71] A. Bobet, H. Einstein, Fracture coalescence in rock-type materials under uniaxial and biaxial compression, International Journal of Rock Mechanics and Mining Sciences 35 (7) (1998) 863–888.

[72] B. Pichler, C. Hellmich, H. A. Mang, A combined fracture-micromechanics model for tensile strain-softening in brittle materials, based on propagation of interacting microcracks, International Journal for Numerical and Analytical Methods in Geomechanics 31 (2007) 111–132.

[73] D. Munson, P. Dawson, et al., A workhardening/recovery model of transient creep of salt during stress loading and unloading, in: The 23rd US Symposium on Rock Mechanics (USRMS), American Rock Mechanics Association, 1982.

[74] M. Aubertin, D. Gill, B. Ladanyi, An internal variable model for the creep of rocksalt, Rock Mechanics and Rock Engineering 24 (2) (1991) 81–97.